Published in final edited form as:
Anal Chem. 2024 May 21; 96(20): 7926–7944. doi:10.1021/acs.analchem.4c01413.

Innovative Approaches for Drug Discovery: Quantifying Drug Distribution and Response with Raman Imaging

Erin L. Dunnington[‡],
Brian S. Wong[‡],
Dan Fu[*]
Department of Chemistry, University of Washington, Seattle, WA, 98195, USA.

Graphical Abstract

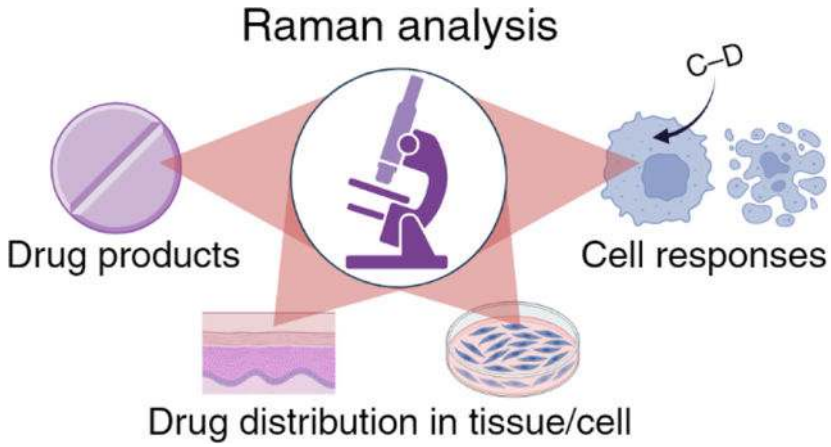

Introduction

Drug discovery and development is a high-cost, high-risk, and time-intensive task, averaging approximately 12 years and $1.8 billion to launch a new drug.[1,2] It begins with the identification of a therapeutic target and culminates in the development of a safe and effective drug. This pathway encompasses numerous stages, including target identification, lead compound discovery, preclinical testing, and multiple phases of clinical trials. Despite the rigorous methodologies employed and the tremendous progress in many pharmaceutical advancements (e.g. targeted therapies for cystic fibrosis, antiviral for Hepatitis-C virus, EGFR inhibitors for lung cancer, etc.) over the past decades, drug development and translation remain challenging with roughly 90% of clinical drug development failing. This does not even account for the failure rate of drug candidates advancing from the preclinical stage to phase I clinical trial.[1,3] Factors contributing to this high failure rate include inadequate efficacy, unforeseen toxicity, poor pharmacokinetics, and challenges

[*]**Corresponding Author**: danfu@uw.edu.
Author Contributions
The manuscript was written through contributions of all authors. All authors have approved the final version of the manuscript.
[‡]These authors contributed equally.

in drug delivery.[1,4] The complexity of biological systems, coupled with the limitations in our ability to predict the behavior of drug molecules within these systems accurately, exacerbates these challenges.

To reduce the attrition rate and accelerate the drug discovery and development process, more human-disease-relevant biological models are needed to quantitatively assess drug pharmacokinetics, pharmacodynamics, drug toxicity, and drug efficacy.[1,5] The traditional *in vitro* 2D cell culture widely used in early drug discovery falls short in recapitulating the complex cell-to-cell interaction and microenvironments found in tissue. Consequently, drugs that appeared promising in simple cell cultures frequently failed in later stages of development due to inefficacy or toxicity in more complex biological contexts.[6,7] Complex *in vitro* models such as spheroids, stem cell- or patient-derived organoids, tissue slices, and organ-on-a-chip are increasingly implemented in the earlier stages of drug discovery and development to identify risk early and validate targets that are more likely to be successful.[8,9] However, the use of these complex models places new requirements on the analytical tools needed to characterize heterogeneous drug absorption, distribution, metabolism, and response. Traditional biochemical assays for measuring these key properties are no longer sufficient as they do not provide any spatially resolved information critical for quantitative analysis and modeling. Chemical imaging, a class of analytical tools capable of generating spatially resolved chemical maps, potentially overcomes these challenges. The most widely used chemical imaging techniques are based on fluorescence, Raman, infrared, or mass spectrometry. Each has unique strengths and weaknesses. Fluorescence-based techniques (e.g., fluorescence microscopy, fluorescence-activated cell sorting, fluorescence-based high-throughput screening, fluorescent sensors, etc.) are commonly used to detect and quantify cell apoptosis, signal transduction, enzyme activity, protein expression, protein binding, and environmental/metabolic changes (e.g. pH or redox state).[10–17] These fluorescence readouts serve as proxies of cellular responses to drug treatment. Direct visualization of drugs is also possible when the drug is naturally fluorescent or tagged with a fluorophore, allowing the study of drug uptake, intracellular trafficking, and target engagement.[18–21] However, fluorescent drugs are uncommon, and tagging small molecule drugs could significantly alter their physicochemical properties.[22,23] In contrast, Raman interrogates the vibrational modes of molecules through the inelastic scattering of light. It is label-free and thus could potentially be used to directly detect many different drugs using their unique vibrational spectra. However, Raman suffers from low cross-section and weak signals. The typical detection sensitivity of Raman is in the millimolar range, compared to the single molecule detection limit of fluorescence.[24–29] Infrared imaging probes molecular vibrations just like Raman. It has higher detection sensitivity but suffers from a severe water absorption background and limited imaging depth.[30,31] The spatial resolution is also much worse. Thus, it is not as widely used as Raman imaging for drug studies. Mass spectrometry imaging (MSI) is a powerful analytical technique that combines detailed chemical analysis from mass spectrometry with spatially resolved mapping, allowing for the visualization of the distribution of drugs, metabolites, lipids, proteins, and other relevant biomolecules in tissue sections.[32,33] Compared to fluorescence and Raman imaging, MSI offers unparalleled specificity and multiplex detection capability, which is essential for studying drug metabolism and understanding

the drug's mechanism of action.[34] The main limitations of MSI are complex sample preparation, destructiveness, difficulty in 3D imaging, and quantification challenges due to matrix effects.[34,35]

In this review, we focus on the application of Raman imaging, especially its advanced form – coherent Raman scattering (CRS) microscopy, in drug discovery and development. As mentioned earlier, the unique ability of Raman to directly probe drug molecules label-free is a major advantage for a wide range of problems from intracellular drug disposition and drug penetration in tissue to drug formulation optimization. However, traditional Raman imaging based on spontaneous Raman effects suffers from several key limitations that prevent its widespread adoption in drug discovery and development, such as its incompatibility with fluorescence, slow imaging speed, low throughput, and poor sensitivity. Many of these limitations can be addressed with advanced Raman imaging techniques, particularly stimulated Raman scattering (SRS) and coherent anti-Stokes Raman scattering (CARS) microscopy, two popular variants of CRS. CRS offers several orders of magnitude higher imaging speed than traditional Raman, thus enabling high-resolution and high-throughput chemical imaging of living biological cells and tissues.[24] These are highly desirable attributes essential for longitudinal tracking of drug uptake, drug distribution, and drug response.

Both spontaneous Raman and CRS have been used to study drug distribution and drug response within biological cells and tissues. Several reviews have covered the application of Raman spectroscopy (RS) and Raman imaging of biological cells and drug distribution.[36–42] Surface-enhanced Raman scattering (SERS) is outside the scope of this review. Rapid advances in CRS imaging in the past decade have catalyzed many biological and biomedical applications, such as tissue diagnosis, lipid metabolism, and drug imaging.[43–45] Many of these technical advances and applications have been reviewed in recent years.[46–55,64] Here, we focus specifically on the contributions of Raman and CRS to drug discovery and development in the last few years. An overview of the topics covered in this review is shown in Figure 1. We target innovations in three application areas: 1. Visualizing and quantifying drug distribution in cells and tissues; 2. Monitoring the metabolic and phenotypic response of drug treatment; 3. Imaging drug formulations to optimize drug stability and drug delivery. In the end, we provide a discussion of the strengths and weaknesses of various imaging approaches and offer our perspective on the future directions of Raman imaging in drug discovery and development.

RS and CRS background, methods, and implementations

RS is an optical technique that interrogates the vibrational modes of molecules through the inelastic scattering of light. This effect manifests as scattered photons losing or gaining energy equal to the vibrational bond energy of a molecule. Typical implementations of Raman imaging would be a confocal Raman microscope, in which a monochromatic laser light source, typically 532, 633, 785, or 1064 nm, is used to interact with molecules at the optical focus. Raman scattered photons are collected by the same objective and separated from the excitation laser with a dichroic mirror and a notch filter. By spectrally separating and detecting these photons with a spectrograph, a Raman spectrum is determined and

used to identify compounds based on their unique vibrational signatures. The technique has gained popularity in drug imaging for its ability to directly analyze drug molecules without the need for labeling. As such, RS-based studies promise a more accurate tracking of drug molecules in their natural environment while allowing for simplified sample preparation. However, the feeble Raman scattering process leads to slow imaging speed, low sensitivity, and poor compatibility with fluorescence. These limitations severely hamper its ability to study living biological systems with high spatial or temporal resolution.

CRS techniques overcome the inefficiency of Raman scattering through coherent excitation of molecular vibrations.[46,24] In CRS, two ultra-short laser pulses, typically denoted as pump (λ_p) and Stokes (λ_S), are focused onto a sample through a high numerical aperture objective lens. At the optical focus, the interaction of the spatially and temporally overlapped two laser pulses generates vibrational coherence when their energy difference matches a molecular vibrational transition ($\lambda_p - \lambda_S = \Omega$). Four coherent Raman processes occur following the vibrational excitation: coherent anti-Stokes Raman scattering (CARS) detected at $2\lambda_p - \lambda_S$, coherent Stokes Raman scattering (CSRS) detected at $2\lambda_S - \lambda_p$, stimulated Raman gain (SRG) at λ_S, and stimulated Raman loss (SRL) at λ_p.[46,56] The detection of the blue-shifted CARS photons can be easily achieved with a photomultiplier tube (PMT) similar to a two-photon laser scanning fluorescence microscope. In comparison, CSRS detects the red-shifted Stokes photons, which is much more difficult due to the overlap with the fluorescence background.[57] In stimulated Raman scattering (SRS), either the SRG and/or SRL effect is detected. The intensity changes due to SRS are small, on the order of 10^{-7}-10^{-4}. Signal collection is often achieved through a modulation transfer scheme with a lock-in amplifier.

Both CARS and SRS microscopy can acquire Raman images at orders of magnitude faster speeds when compared to spontaneous RS approaches. Fluorescence interference is typically less of a concern. Compared to SRS, CARS microscopy suffers from a broadband non-resonant background that arises from an electronic four-wave mixing process.[46] This ubiquitous background distorts the Raman spectrum, complicates concentration determination, and degrades sensitivity. Some of these CARS limitations can be overcome with the maximum entropy method or Kramers-Kronig transform to reconstruct real Raman spectra.[58–60] However, a large spectral range is needed, which places constraints on the laser bandwidth and imaging speed due to the slow camera-based spectral acquisition. In comparison, SRS is free from the non-resonant background due to the requirement of vibrational excitation.[24] The signal scales linearly with concentration, facilitating straightforward quantitative analysis.[61] However, SRS requires modulation and phase-sensitive lock-in detection, which increases the complexity of the setup. Moreover, a low-noise laser is typically required, making the use of low-cost fiber laser and supercontinuum generation difficult. As a result, it also suffers from the limited bandwidth of solid-state lasers and the resulting narrower spectral range compared to broadband CARS imaging.[62] Despite these limitations, since the initial demonstration of SRS, it has been gaining popularity owing to the aforementioned advantages over CARS. Signifying this popularity, SRS has seen tremendous technological development in recent years, providing unprecedented measurement capabilities, such as temperature measurement, pH measurement, biorthogonal probes, super-multiplex imaging, and single virus detection, etc.[63–69]

Imaging drug molecule distribution and delivery in cells and tissues

Direct imaging of cellular drug uptake and distribution

Many drug molecules have distinct Raman bands that facilitate their direct imaging and quantification in biological cells. In particular, drugs with vibrational signatures in the silent Raman window from 1800–2700 cm^{-1} can be readily separated from the cellular background. This is commonly achieved with either deuterium labeling or small Raman tags such as alkyne (-C≡CH) and nitrile (-C≡N). Some drugs already have the alkyne or nitrile group. For instance, El-Mashtoly *et al.* achieved subcellular imaging of erlotinib using confocal RS in 2014, integrating RS intensity of the C≡C bond (2085 to 2140 cm^{-1}) as a label-free drug marker in colon cells.[70] Later, Aljakouch *et al.* applied a similar approach to study the spatial distribution of neratinib, which has a nitrile group at 2208 cm^{-1}.[71] In both studies, computational modeling was applied to RS spectra for metabolite discovery. Imaging in the fingerprint region is possible when drugs have high local concentrations and/or large Raman cross-sections. LaLone *et al.* developed a RS screening platform to measure the drug loading of nilotinib across time within macrophages.[72] More recently, Koga *et al.* investigated the intracellular distribution and condensation of poorly water-soluble drug molecules, focusing primarily on all-trans retinoic acid (ATRA).[73] By normalizing the RS intensity of ATRA (C=C at 1580 cm^{-1}) to extracellular water, quantitative visualization of ATRA concentration within single cells over different incubation times was achieved. These studies showcase RS's capabilities in investigating subcellular drug pharmacokinetics and metabolism in a label-free manner. However, spontaneous Raman imaging faces limitations in speed, often on the order of many minutes to hours, constraining imaging mostly to fixed cells.

Compared to spontaneous Raman, SRS microscopy enables quantitative, rapid, non-perturbative, and high-resolution chemical imaging of small-molecule drugs in live biological cells. This powerful capability was demonstrated by Fu *et al.* in an early study of the quantitative distribution of tyrosine kinase inhibitor (TKI) drugs imatinib and nilotinib in cultured leukemia cells.[26] They showed that the unique Raman signatures of these drugs in the fingerprint region 1200–1500 cm^{-1} can be used to quantify their concentrations at submicron spatial resolution through linear regression. They measured over 1,000-fold enrichment of the drugs in cell lysosomes. Moreover, they demonstrated direct imaging of synergistic drug-drug interactions by observing the absolute concentration changes of two different drugs, imatinib and chloroquine. Similar SRS imaging strategies of live cells have been employed in several later studies investigating the uptake of other TKI drugs, including ponatinib[74] and 7RH[75]. In both cases, the intrinsic C≡ C vibration was used for SRS drug imaging.

It is important to note that the SRS detection sensitivity is limited to low millimolar concentrations while many drug dosages are at micromolar levels, far below the detection limit. Therefore, SRS can only detect drugs that are highly enriched in cellular compartments. It is well-established that weakly basic drugs are selectively accumulated and trapped in acidic organelles, especially lysosomes, due to acid-base thermodynamic equilibrium.[76–78] This common effect facilitates the imaging of many different drugs,

particularly kinase inhibitors, a large fraction of which are weakly basic. Enrichment of drugs in other organelles such as mitochondria may also allow SRS to overcome the detection sensitivity limit.[79,80] Engineered Raman tags offer a potential route to increase detection sensitivity. They were first introduced by Yamakoshi *et al.* in 2012 and developed to target low molecular weight compounds with minimal perturbation.[81] Since then, Raman tags have seen widespread development as multiplexable Raman probes.[64,66–68] Bae *et al.* synthesized mitochondria-targeting compounds and used SRS to monitor real-time cellular accumulation.[82] They found that a reduction in the mitochondrial membrane potential causes significant decreases in both the uptake rate and intracellular concentrations of their mitochondria targeting agent. Yuan *et al.* developed drug-like compounds to directly characterize lysosomal sequestration of drugs and their influence on cell functions with SRS.[83] They studied the internalization of lysosomotropic compounds and their influence on lysosomal metabolism. Despite these efforts, direct tagging of drugs still requires enrichment due to low sensitivity. Even in the best case, detection sensitivity is in the hundred micromolar range for small alkyne tags.[84]

The quantification capability of SRS imaging can be used to further investigate drug uptake mechanisms. Oda *et al.* applied SRS for real-time visualization of an anesthetic, propofol, and monitored the dynamics of propofol binding in neuron cells.[85,86] Dong *et al.* used SRS to understand the orientation of amphotericin B (AmB) in pathogenic fungi using polarization-sensitive SRS.[87] The authors visualized the distribution of AmB by targeting fingerprint C═C stretching vibrations at 1556 cm^{-1} and 1602 cm^{-1} (Figure 2a.i–ii.) and revealed that AmB distribution is highly ordered. AmB was found to primarily be oriented parallel to the laser polarization direction and perpendicular to the axis of CH2 groups in the membrane (Figure 2b), supporting the classical ion channel model in which AmB vertically forms transmembrane tunnels. Wong *et al.* utilized SRS microscopy to study the intracellular uptake dynamics of several lysosome-sequestering epidermal growth factor receptor (EGFR) inhibitors, including lapatinib, afatinib, gefitinib, and osimertinib.[88] By spectrally unmixing the drug and cellular components in the 1400–1600 cm^{-1} fingerprint region, they were able to quantify the intracellular concentration of TKIs (Figure 2c). By perturbing facilitated drug transport through organic cation transporters (OCTs) and ATP-binding cassette (ABC) transporters with known transporter inhibitors, they determined that OCT1 and ABCB1 transporters play an important role in lapatinib and afatinib transport.

Collectively, both RS and CRS studies highlight the potential of quantitative Raman imaging to reveal drug uptake, distribution, and metabolism at subcellular resolution. To overcome the challenge in sensitivity, current research takes advantage of the organelle enrichment of drugs to push concentrations into the millimolar range or target drug compounds with high Raman cross-section (e.g. conjugated C=C bond). The cytosolic concentrations of drugs without enrichment remain out of reach. Understanding drug metabolism is another challenging task due to the often-unknown changes of drugs inside cells or significant spectral overlap between drugs and their metabolites. Given that ~50% of FDA-approved kinase inhibitor drugs are weakly basic and enriched in lysosomes, Raman imaging will continue to play a role in understanding pharmacokinetics at the cellular and subcellular level. Such a capability will become more important as studies move beyond simple 2D cell

culture to more disease-relevant complex 3D cultures with large cell-to-cell heterogeneity, including 3D spheroid, organoids, tissue slices, or organ-on-a-chip.

Imaging drug penetration in tissue and transdermal delivery

Imaging drug distribution in tissue presents additional challenges compared to cellular imaging. Although RS and CRS microscopy can retain subcellular resolution, the signal decays rapidly with tissue imaging depth due to light scattering. Confocal Raman imaging is reported to have a typical imaging depth of ~100 um in tissues, varying based on wavelength, configuration, and sample.[89,90] CRS imaging depth has been reported to be higher, reaching 300 μm in brain tissue.[91,92] Optical clearing improves imaging depth but likely disrupts drug distribution.[93]

With confocal Raman imaging, Woodhouse *et al.* quantitatively detected alkyne- and isotope-tagged drug molecules in rat liver and brain biomimetic tissue models.[94] The tissue was sectioned very thin (~16 μm) to minimize out-of-focus fluorescence. After normalization to a calibration curve for each given drug/tissue combination, alkyne-tagged drugs were measured at 34 ± 6 μg/g drug/tissue mass ratio in liver, and 18 ± 5 μg/g in rat brain. This study showcased the ability to quantify small-molecule drugs in tissues such as the liver that are highly auto-fluorescent under laser illumination.[94] The drug signatures in the Raman silent region exhibited a lower fluorescent background compared to the fingerprint region. In renal tubules, Sperati *et al.* identified the spectroscopic signature of intratubular triamterene crystals, a diuretic that is linked to kidney stone formation.[95] Spencer-Dene *et al.* combined CARS imaging with an miRNAscope In Situ Hybridization (ISH) assay and CARS imaging to monitor the distribution of bepirovirsen in murine kidney and liver tissues.[96] While a few studies have explored direct imaging of drugs in internal organ tissue, the overwhelming majority have focused on the skin. This is likely due to the accessibility and integrity of skin tissue samples and their ease of preparation for imaging.

Permeation into and/or through the skin is vital for the delivery of topically applied drugs to their intended sites of action. Drug molecules must penetrate through the skin's lipid-rich stratum corneum (SC) layer (10–20 μm in humans) to the viable epidermis and dermis tissue beneath or even to the bloodstream to be distributed systemically throughout the body (transdermal delivery).[97,98] Observing and measuring the interactions between drugs and the skin, as well as the dynamics of permeation, reservoir formation, and sustained release, indicate how well a formulated product delivers the drug to its intended site at effective concentrations. Methods to evaluate such processes *in vitro* (Franz diffusion cell) or *in vivo* (i.e. skin biopsy or tape stripping method) are often variable, difficult to reproduce, require long measurement time, and are highly invasive or disruptive to the skin layers.[99] In contrast, non-destructive Raman-based drug imaging, despite its limited imaging depth, can probe drug permeation through the thin SC and epidermis layer.

Raman imaging has been implemented for direct, quantitative mapping of drug compounds in topical formulations and their delivery into the skin and appendages.[100–103] For example, drug delivery and absorption events were interrogated at the interface between porcine skin and (trans)dermal formulations.[104] A depth profile of nicotine penetration into the SC after patch application indicated that nicotine transport was nearly steady-state after being applied

for 2 h. Raman mapping was also used to characterize unwanted fentanyl structural and chemical changes when the adhesive delivery system was improperly used.[105] For topical drugs that localize in the skin, RS has been utilized to characterize bioavailability within the targeted area. Zarmpi *et al.* employed confocal Raman imaging to identify the strongly Raman-active model skin penetrant 4-cyanolphenol (CP) at least 10–40 μm into the skin, below the SC.[106] Using amide I signal from keratin in skin tissue, they were able to normalize the drug signal with respect to imaging depth when collected "top-down". This method was used to assess depth-dependent CP uptake (1, 2, or 6 h) and clearance (after 6 h of uptake) from multiple CP-containing formulations. Further studies using CP have focused on chemometric spectral unmixing methods to quantify depth-dependent permeation of CP into the skin[107] and a comparison to direct quantification of SC drug content with tape-stripping procedure[108]. Recently, time-dependent uptake and distribution of CP were measured using SRS imaging to provide improved depth resolution compared to confocal Raman.[109]

CRS imaging offers a robust approach for real-time quantitative analysis of cutaneous pharmacokinetics with different tissue models. Sarri *et al.* applied CARS and two-photon excited auto-fluorescence to image the penetration of high concentrations of deuterated glycerol in *ex vivo* and *in vivo* skin.[110] They found that xanthan gel retains glycerol on the skin surface for constant release. Ito *et al.* developed an innovative phase-modulated (PM)-SRS scheme to improve low-concentration drug detection and measured penetration of a skin moisturizing agent, an anesthetic, and a nonsteroidal anti-inflammatory *in vitro*.[111] With their PM-SRS, they demonstrated 40 times higher signal contrast compared to conventional amplitude-modulated SRS. PM-SRS further revealed a detailed spatial and temporal pharmacokinetic profile at the tissue surface layer over 240 min through mean intensity change at the 1184 cm^{-1} (C−C stretching) Raman shift of loxoprofen (Figure 3a).

Feizpour *et al.* combined SRS and deep learning to model the diffusion and uptake of topical drugs through skin tissue.[112] Convolutional neural networks were trained to identify regions of the drug of interest. By monitoring drug distribution over time, they were able to quantitatively track drug penetration kinetics through different skin layers. Kuzma *et al.* further studied cutaneous pharmacokinetics through the development of a 3D-printed microfluidic device compatible with CRS imaging for relative concentration monitoring following drug product application.[113] This platform was utilized to measure ruxolitinib uptake concentration-time profiles of two formulations into layers of frozen nude mouse ear skin. Recently, Iliopoulos *et al* employed SRS to assess the permeation of tazarotene, a topical retinoid, through various skin microstructures.[114] By scanning the 1590 cm^{-1} band for tazarotene and the 2870 cm^{-1} lipid band for skin structure, they were able to visualize and quantify drug permeation over time (Figure 3b). With their pharmacokinetic imaging method, drug bioavailability within different skin layers was successfully quantified and allowed for the first assessment of bioequivalence among various topical formulations with similar active pharmaceutical ingredient (API) content. CRS has also been combined with other label-free quantitative imaging methods for drug detection and qualifying drug exposure-induced tissue structure changes.[115,116]

The diverse drugs studied *in vitro* and *ex vivo* highlight the potential of CRS for studying the pharmacokinetics of various drug and formulation products applied topically. However, several limitations remain. The strong tissue scattering limits the imaging depth in the skin to the dermal-epidermal junction and the upper dermis layer. Tissue clearing can enhance the imaging depth but it may interfere with drug permeation.[93] Few APIs have distinct Raman peaks; thus, Raman imaging and CRS of drugs often suffer from spectral interference from formulation ingredients and tissue background signals. Raman tagging in the silent window and advanced data analysis tools may help mitigate these challenges.

Imaging nanocarrier-based drug delivery

Many drugs have difficulty penetrating tissue to reach their targets. This is particularly challenging for central nervous system diseases (CNS) due to the presence of the blood-brain barrier (BBB).[117] Nanoformulations, which are drug delivery systems featuring engineered encapsulation of drug cargo, promise significant enhancements of pharmacological profiles, drug circulation, membrane transport, and target specificity.[118] Examples of FDA-approved drugs include liposome-based nanoformulations Onivyde and Doxil Caelyx.[119] More recently, lipid nanoparticles were the technological basis for the development of successful COVID-19 vaccines.[120] Tracking drug delivery through nanocarriers is a challenging task. Commonly used fluorescent tagging of nanoparticles can alter nanoformulation efficacy.[22,23] Label-free chemical imaging of the nanocarrier offers an alternative approach to examining cargo loading, targeting, and release.

RS has been used to investigate nanocarrier properties.[42,121–124] Penders *et al.* developed an imaging platform method called Single Particle Automated Raman Trapping Analysis (SPARTA) for the label-free, nondestructive analysis of nanoparticles.[125] The platform combined optical trapping with Raman spectroscopy to characterize the composition, size, and dynamic processes of individual nanoparticles at high throughput. The authors successfully demonstrated the advanced capabilities of SPARTA by analyzing different nanoparticle formulations, including liposomes and polymersomes as well as the functionalization of polystyrene particles. Since its initial demonstration, SPARTA has been used to study a multitude of nanoparticle systems in recent years.[126–128] Saunders *et al.* adapted SPARTA to distinguish cargo location and loading heterogeneity within nanoparticle populations.[129] They generated a theoretical model and showed a positive, linear correlation between the encapsulating polymer and cargo mass for membrane loading and a much lower, cubic relationship for core loading. This relationship allowed them to introduce a semiquantitative test to distinguish these loading behaviors (Figure 4a).

For tissue imaging, it is necessary to have fast imaging capability to identify the sparse distribution of nanocarriers. CRS techniques have emerged as a powerful tool to quantitatively image nanoparticle distribution in tissue. In 2018, Godfrey *et al.* showed the first demonstration of CARS to investigate the distribution of nanoparticle delivery to the brain through a nasal route.[130] The authors dosed rats with deuterated GCPQ and revealed the distribution of nanoparticles by scanning the 2100 cm^{-1} C−D band across several brain regions. Bera *et al.* utilized CARS microscopy and fluorescence life-time imaging microscopy to probe the delivery and distribution of self-amplifying mRNA (SAM) lipid

nanoparticle (LNP) vaccine delivery.[131] CARS was used to visualize and quantify the spatial biodistribution of SAM-LNPs within cells, by focusing on the lipid-rich regions in the 1400 – 1600 cm−1 fingerprint region. With their multimodal imaging method, the authors demonstrated that uptake of SAM required around 5 h. Additionally, it was also possible to classify empty LNPs and SAM-LNPs with ~90% accuracy from the lipid:protein ratio from CARS spectral information.

Vanden-Hehir *et al.* synthesized polymeric NPs and visualized their uptake in *ex vivo* murine brains with SRS.[132] Specifically, the authors synthesized two Raman-active Poly(lactic acid-co-glycolic acid) (PLGA) analogs, namely PLGA-D (deuterium-labeled) and PLGA-alkyne (alkyne-labeled). These analogs were then fabricated into nanoparticles and their distribution was characterized by SRS. The SRS images demonstrated the internalization of these nanoparticles, particularly PLGA-alkyne, by primary rat microglia over a 24-h period, with no observed toxicity. Additionally, with *ex vivo* mouse brain slices, widespread distribution of alkyne-labeled nanoparticles was observed throughout the tissue. Most recently, Gao *et al.* applied SRS microscopy to visualize PLGA nanoparticles with single-particle sensitivity.[133] The authors identified a distinct ester vibrational with PLGA at 1768 cm^{-1} that allowed label-free detection of PLGA nanoparticle distribution across different biological systems such as macrophage cells, skin, tumors, and liver. With their single-particle imaging capability, Wei *et al.* recently applied SRS to track and quantify nanoformulations entering the brain across different brain regions (Figure 4b).[134] By monitoring the characteristic peak of poly(n- butyl cyanoacrylate) nanoparticles at 2249 cm^{-1}, the authors were able to generate several unique metrics from single-particle tracking to determination of the number of nanoparticles crossing the BBB, the number of nanoparticles in each cell type across different brain regions, and the heterogeneity of BBB transport with respect to age.

Although nascent, the exciting advancement of CRS technologies to look at nanocarriers for drug delivery opens new avenues to study and improve nanoparticle-based drug delivery systems. Research to date has focused on imaging the nanocarrier itself instead of the drug due to its stronger signal. Simultaneously tracking drug delivery within cells, although challenging, could be transformative in better understanding drug delivery and optimizing nanoformulations.

Imaging drug response through biochemical and metabolic changes

Monitoring drug-induced biochemical response

While direct imaging of drugs offers valuable insights in mapping drug distribution and studying drug transport, this approach does not work for drug concentrations below the detection sensitivity. Additionally, given the complexity of the biological environment, the drug Raman spectrum could heavily overlap with native biomolecules, leading to difficulty in quantifying drug concentration even if sensitivity is not a problem. Instead, by leveraging the chemically rich information contained within Raman spectra, the examination of changes in cellular content such as lipid, protein, and nucleic acid at a sub-cellular scale in response to drug treatment is an alternative to understanding drug dynamics.[38,135] A multitude of studies have been published in recent years on applying RS to identify biomarkers and biochemical changes associated with drug treatments.[136–145] For example,

Hammoud *et al.* explored the impact of EGFR mutations on cellular responses to different TKIs.[146] By identifying differences in Raman spectra before and after drug treatment, large spectral changes were detected that indicated alterations in cellular composition. Later, they employed RS microscopy in combination with a deep wavelet scattering-based multivariate analysis framework to evaluate the potency, effectiveness, and distribution of lapatinib and neratinib in breast cancer cells.[147] This approach discriminated between control cells and drug-treated cells with high accuracy, demonstrating significant changes in the spectra of drug-treated cells, particularly in regions associated with lipids, proteins, and nucleic acids. Furthermore, colocalization analysis of RS spectra combined with fluorescence imaging revealed the distribution of lapatinib that binds to EGFR and HER2 receptors. Yay *et al.* used RS to analyze kidney tissue damage by antioxidants and cisplatin.[148] Cao *et al.* applied RS to assess the efficacy of obeticholic acid and gigantol for treating liver fibrosis.[149] Li *et al.* monitored drug-induced cytotoxicity and detected cytotoxicity earlier than MTT assay with RS.[150]

Despite the potential demonstrated by these studies, as mentioned earlier, RS is hindered by slow image acquisition speeds rendering large datasets difficult to acquire. As such, efforts have been made to increase the throughput of drug studies by developing new RS-based platforms. For example, LaLone *et al.* developed a Raman cytometric platform to measure cell content at picogram scale.[151] The authors accomplished this by creating single-cell-sized micro-calibration standards of known composition. Using an inkjet printer to deposit biomolecular components to make microarrays across the surface of silicon chips, the authors were able to monitor phospholipidosis for cells treated with amiodarone. Later, they developed a quantitative Ramanomics (qRamanomics) approach for detailed analysis of 3D liver models in response to drug exposure.[152] Their approach involves a robust data-processing and calibration pipeline, allowing the label-free, multi-factorial, chemometric phenotyping of biospecimens through confocal Raman imaging. With qRamanomics, their compared drug response of 3D primary human hepatocytes (3D PHH) and induced hepatocyte-like cells (3D iHLC), revealing distinct differences in lipid distribution and colocalization of other major biomolecules across drug treatment (Figure 5a). Furthermore, the platform enabled the mapping of biochemical and drug components within organoids at high resolution (Figure 5b). Importantly, this study demonstrates the capability of RS to monitor phenotypic alterations in the biochemistry of cells without requiring any tagging.

Kawagoe *et al.* developed a multiwell Raman plate reader for high-throughput biochemical screening.[153] By employing an array of high numerical aperture lenses positioned beneath each well of a standard multiwell plate, they parallelized RS data acquisition to achieve 100-fold speed improvement compared to serial acquisition. With this system, the authors studied drug polymorphism, alkyne-tag screening, and mapped large samples. An adaptation of the multiwell RS system was used in 2023 to examine drug-induced cellular changes in 3D cell spheroids.[154] They investigated biochemical changes of HeLa and HepG2 spheroids subjected to Actinomycin D (ActD) and Free Fatty Acid (FFA) treatments, respectively. In ActD-treated HeLa spheroids, Raman spectra revealed dose-dependent changes with a significant increase in the Raman intensity at 1485 cm^{-1}, and a decrease in the Raman intensity at 1585 cm^{-1} was observed with ActD treatment at a concentration range of 0.3–10 μM (Figure 5c.i–iii.). Notably, 3D spheroids exhibited greater resistance to ActD

compared to their 2D cultured counterparts. In the FFA-treated HepG2 studies, Raman spectra exhibited concentration-dependent alterations, including lipid accumulation and cytochrome oxidation. A positive correlation between the intensity at 1445 cm^{-1} and FFA concentration was observed, indicating FFA concentration-dependent lipid accumulation in the hepatocytes. These findings were validated with cell viability assays, confirming the capability of RS to capture cellular responses.

Compared to RS, CRS typically has a much narrower spectral range, and the majority of studies focus on the C–H region (~2800–3050 cm^{-1}) due to high signal intensity. Masia *et al.* demonstrated the capability of hyperspectral CARS microscopy in the C–H region to screen 15 combinations of drugs and lipids in a liver cell line.[155] Through the sparse sampling of wavenumbers and spatial x-y, coupled with the utilization of a Bessel beam for high-throughput imaging and a support vector machine (SVM) for the discriminative classification of drug response, the authors successfully distinguished two deleterious drug-induced liver injuries — steatosis and phospholipidosis. Similarly, Tipping *et al.* in 2022 showed that C–H SRS imaging with spectral phasor analysis could be used to observe drug-cell interactions of different statins, an inhibitor of 3-hydroxy-3-methylglutryl coenzyme A (HMGC) reductase that is prescribed to lower cholesterol levels.[156] By projecting the SRS spectrum spanning the C–H region from each pixel within the hyperspectral stack onto a two-dimensional phasor plot, they revealed differences in intracellular lipid content in breast cancer cell lines after drug treatment with atorvastatin and rosuvastatin. In a subsequent study, Hislop *et al.* analyzed the effect of an acetyl-CoA carboxylase inhibitor TOFA on lipid droplets (LDs) in prostate cancer cells with SRS microscopy and multivariate analysis.[157] The study revealed an over-reliance of prostate cancer cells on *de novo* lipid synthesis for metabolic requirements from the significant reduction in LD content after TOFA treatment, which was not observed in normal prostate cell models. Baek *et al.* used SRS to observe the drug-induced effects of their synthesized novel chalone drug.[158] They found that treated cells were blebbing and accumulated lipid-like substances, indicative of drug-induced apoptosis. Additionally, Zhang *et al.* utilized SRS imaging in the fingerprint region to identify ergosteryl ester as a marker of azole-resistant *Candida albicans* by probing lipogenic pathways in drug-susceptible and resistant strains.[159]

The spectral change in the C–H region, although reflecting underlying lipid, protein, and nucleic acid compositions, is often subtle and ambiguous due to the lack of sharp spectral features as seen in the fingerprint region. To better leverage these subtle changes for drug studies, new efforts have been made to apply more sophisticated deep-learning approaches to understand spectral change at a subcellular level after drug treatment. *Shi et al.* used hyperspectral-CARS microscopy in conjunction with a weakly supervised deep learning model to investigate the effects of an antisense oligonucleotide drug, bepirovirsen, in murine cells.[160] They developed a hyperspectral attention net (HAN) to identify informative spatial regions at a subcellular level in tissue imaging data. HAN highlights the spatial areas indicating drug-induced changes as seen in Figure 5d.i. It was observed that the 2900–3050 cm^{-1} spectral range revealed patterns correlating with HAN attention scores (Figure 5d.ii.). Interestingly, the informative areas predicted by HAN had a high degree of similarity with *in situ* hybridization staining, supporting the capability of HAN to reveal drug-induced biochemical changes.

Drug-induced senescence is another area that has been explored with SRS imaging. Oh *et al.* introduced a quantitative SRS technique called normalized Raman imaging (NoRI) in 2022.[161] The basis of NoRI lies in its normalization algorithm in which SRS intensities at 2935 cm^{-1} (protein), 2853 cm^{-1} (lipid), and 3420 cm^{-1} (water) peaks of pure species are used to create a 3×3 calibration matrix. By applying this calibration matrix to normalize scattering-dependent signal loss, the authors were able to precisely quantify the water, protein, and lipid mass within cells and tissues. They measured absolute cellular content changes of live MDCK and A7 cells treated with doxorubicin. Both cell lines showed a significant reduction in cytoplasmic dry mass and protein concentrations in senescence compared to proliferating interphase cells. In 2023, Bresci *et al.* combined CARS and SRS with quantitative phase microscopy to investigate cell senescence.[162] The authors found alterations in cell volume, thickness, and dry mass in the HepG2 cells following deferoxamine- or radiation treatment. Lipid droplet characteristics, such as volume and dry mass, also exhibited notable changes during treatment, indicating senescence manifestations as early as 24 h after treatment.

Overall, RS and CRS are shown to be able to detect drug-induced biochemical changes in a label-free manner without prior knowledge. RS offers rich chemical information with low throughput, while CRS provides high-speed imaging at submicron spatial resolution, albeit limited to the C–H region in most studies. In either case, monitoring biochemical changes typically involves developments in machine learning and deep learning methods to extract key differences in biochemical content within cells. The use of absolute concentration through normalization procedures as shown in NoRI facilitates comparison across many different cell types and conditions. We expect that further developments in advanced data processing and acquiring additional chemical features promise a more unbiased and comprehensive understanding of drug-induced biochemical changes. These developments will facilitate the adoption of Raman imaging for high-content drug screening in both 2D cell cultures and complex 3D tissue cultures.

Tracing metabolic changes in response to drug treatment

Besides monitoring the overall biochemical changes of proteins, lipids, and nucleic acids, a more specific approach to monitoring drug response is to quantify metabolic changes through stable isotope tracing. Stable isotopologues containing ^{13}C, ^{2}H, etc. are often utilized in Raman-based imaging to track metabolic pathways.[163] With small mass changes, these compounds retain a similar structure and size without altering their cellular metabolic functionalities yet provide enhanced chemical contrast by shifting the vibrational frequency to a position that is distinct from endogenous molecules. In particular, deuterium tracing is most commonly used because it shifts the Raman peak to the cell-silent spectral region, enabling sensitive detection without cell background interference.[39,164] This method is attractive for tracing the distribution and localization of newly synthesized proteins, lipids, and other biomolecules in single cells through the uptake of labeled metabolic substrates such as glucose or water.[165] Drug molecules perturb these metabolic processes and thus drug response can be indirectly probed through Raman imaging of metabolically incorporated isotope labels.

With confocal Raman imaging, deuterium isotopic probing has been used to reveal drug-induced metabolic response heterogeneity in cancer and fungal cells and determine antimicrobial drug sensitivity. Hekmatara *et al.* investigated organelle-level biosynthesis in rapamycin-treated yeast and cancer cells with deuterated water.[166] Their findings revealed differential protein and lipid metabolic activity in the cell compartments in response to treatment. For example, *de novo* protein biosynthesis was highly active within the nucleus of cancer cells and *de novo* lipogenesis was inhibited in cancer cells, while the activity of both was inhibited in the lipid bodies. Meanwhile, syntheses of both biomolecules were dose- and duration-dependent in the cytoplasm. More recently, Zhao *et al.* developed a technique to utilize multiplexed vibrational probes for single-whole-cell mapping of metabolic fluxes.[167] Cell culture medium was supplemented with deuterated branch-chained amino acids and deuterated palmitic acid to probe protein and fatty acid metabolism, respectively. Concentration profiles were constructed through the decomposition of the composite spectra into the distinct, pure spectra of the deuterated probes. The application of these tags directly measured the activity of the two pathways in response to treatment with five drugs with known metabolic inhibitory effects. Raman-based susceptibility testing has been introduced for rapid, label-free identification of an effective antimicrobial drug and dosage for bacterial colonies. Deuterated probes, such as water, are ideal for this application due to their compatibility with complex clinical urine and blood samples.[168] Yi *et al.* developed a fast Raman-assisted susceptibility test (FRAST) to detect single bacterial metabolic activity when treated with antibiotics.[169] The authors found an overall agreement of 88% between conventional susceptibility testing and FRAST for four Gram-negative and two Gram-positive bacteria strains in response to 38 antibiotics.

CRS imaging methods provide similar capabilities but at much higher throughput. SRS imaging has shown to be a powerful tool for rapid antimicrobial susceptibility testing.[170–174] For example, Chen *et al.* developed a metabolic imaging method to determine antifungal susceptibility within 4 h.[175] By monitoring the intracellular conversion of D_2O or glucose-d_7 to C–D bonds in proteins, lipids, and DNA, the authors successfully demonstrated the use of metabolic change as a marker for rapid susceptibility testing (Figure 6a.i). The antifungal drug amphotericin B was found to inhibit metabolism at high concentrations (≥1 μg/mL) by monitoring the average cellular C–D intensity. By comparing to the SRS intensity of the untreated cells, a C–D ratio of 0.55 was determined to be the threshold for determining the single-cell metabolic change concentration (lowest concentration of drug to detect significant metabolic change) for this drug and cell strain (Figure 6a.ii). In contrast, other antifungals, including fluconazole and voriconazole, stimulated metabolism at high concentrations. Drug susceptibility of bacteria was monitored through D_2O incorporation.[176] Metabolic response was observed within 10 min after medium supplementation with 70% D_2O. The authors determined a minimum inhibitory concentration for 36 different bacterial samples.

Alongside antimicrobial susceptibility testing, SRS microscopy has been implemented to profile anticancer drug response in cultured 2D cancer cells and 3D spheroids. Huang *et al.* presented high-throughput multiplex SRS imaging cytometry to study single pancreatic cancer cell metabolic response to starvation and gemcitabine-induced stress conditions.[177] Their findings indicated that stress-resistant pancreatic cancer cells contained protrusions

high in lipid content for local energy production. Tan *et al*. identified reprogramming in cisplatin-resistant cancer cells from glycolysis-dependent to fatty acid beta-oxidation-dependent anabolic metabolism.[178] The authors found that cisplatin treatment induced a metabolic shift to increased fatty acid uptake of palmitic acid-d31 and oleic acid-d34 instead of increased lipogenesis. Xu *et al*. used deuterated essential amino acids to quantify single-cell growth rates as a ratio of the incorporated C–D bonds from newly synthesized labeled proteins and the total C–H bonds from unlabeled proteins.[179] With ratiometric C–D/C–H SRS, they observed variations in metabolic and morphological response to different drugs, including the TKIs gefitinib and lapatinib as indicated in Figure 6b.i., as well as paclitaxel and etoposide. Using data from hundreds of single cells at each drug concentration, they were able to obtain a half-maximal inhibitory concentration (IC_{50}) that is consistent with the MTT assay. Interestingly, they observed potential concentration-dependent subpopulations in response to lapatinib, indicating potential cellular heterogeneity within the monoculture of isogenic cells. A major advantage of the ratiometric SRS method is that it applies to 3D cell culture (Figure 6b.ii.). The authors measured cell growth rate in 3D tumor spheroid treated with gefitinib and observed much higher IC_{50} compared to 2D culture, suggesting that drug sensitivity strongly depends on the microenvironment of the cells. The single-cell drug response measurement capability offers distinct advantages compared to traditional cell viability assays, especially when it comes to complex 3D cell culture. Traditional assays only provide the average response of the sample and do not account for cell heterogeneity or detect subpopulations of cells with differential drug responses.

Compared to biochemical composition changes, metabolic changes offer higher specificity in drug response, especially when specific and/or multiple metabolic pathways are probed. However, they are intimately related as metabolic change gives rise to compositional change. Deuterium tracing facilitates the extraction of dynamic and small changes that may be difficult to observe with overall biochemical composition. The use of D2O as a metabolic substrate, as shown in antibacterial and antifungal drug testing, offers a convenient readout. However, mammalian cells cannot tolerate high concentrations of D_2O. Their growth is also much slower, which makes the use of D_2O for drug response monitoring more challenging. Nevertheless, the availability of other deuterated substrates, including sugar, amino acids, and lipids, offers many possibilities for drug response measurements with RS and CRS. Most of these studies to date are still focused on cultured cells. However, extending measurements of drug-induced metabolic changes to complex tissue models such as patient-derived organoids is entirely feasible and will be interesting to explore in the near future.

Imaging dynamic changes in drug formulations

Outside biological samples, Raman-based techniques have increasingly been utilized in characterizing pharmaceutics formulations.[180,181] When drugs are taken up into the body, pharmacokinetics, including drug absorption, distribution, metabolism, and excretion, can be significantly impacted by drug formulation. Drug formulation comes in a wide variety of formats, such as solid tablets, capsules, injectables, implants, etc. Chemists tend to focus on the active pharmaceutical ingredients (API), but drug formulations also contain many other excipients such as lubricants, binders, and diluents to improve drug stability

and bioavailability. Raman imaging is highly versatile in the analysis of various types of pharmaceutical dosage forms ranging in opacity, pigment, physical state, and sampling configuration.[180]

Pharmaceutical formulations typically have well-defined APIs and excipients. Due to its inherent specificity, Raman imaging has shown to be useful in the analysis of solid pharmaceutical samples and the classification of different APIs and their structures.[182–189] Importantly, Raman can also be used to characterize chemically identical forms of an API that differ in crystalline lattice structures or molecular conformations known as polymorphs. Polymorphism plays an important role in drug dissolution, thermodynamic stability, and API bioavailability.[181,190] Grand *et al.* developed a fast Raman imaging technique using compressive sensing for rapid characterization and mapping of clopidogrel polymorphs and three excipients in tablets with a pixel dwell time of 2.5 ms.[191] Fateixa *et al.* identified the transition of carbamazepine p-monoclinic into carbamazepine triclinic after heating treatment.[192]

One of the challenges of imaging solid dosage forms is strong light scattering and shallow imaging depth with Raman. Tablets are usually sectioned while powders are pressed to provide relatively uniform backscattering signals. Alternatively, reflection-based feedback mechanisms for focus tracking have been used for curved, non-flat surfaces.[193] The surface imaging capability of Raman is suitable for investigating drug surface coating. For example, carnauba wax dry-coating heterogeneity and thickness on paracetamol particles were analyzed with confocal 3D Raman mapping (Figure 7a.i).[194] The inner structure of multiple particle size fractions was characterized per pixel, where each pixel is color-coded based on its correlation to pure Raman spectra of paracetamol and carnauba wax (Figure 7a.ii). The authors found that regardless of particle size, the coating had variable thickness at 5.9 ± 4.2 μm. The coating was found to be either intact wax particles stuck on the surface or deformed particles spread along the surface. Interestingly, increased particle size and tableting lead to slower API dissolution as less surface area was exposed to the dissolution medium.

Due to the shallow imaging depth, Raman or fluorescence signals from the capsule shell or surface coating tend to dominate signals from subsurface components. Interrogating internal matrix content is important for evaluating layered structures and identifying inhomogeneities or defects in the inner core.[195] Serial sample sectioning and image reconstruction have been used to achieve 3D volumetric mapping of tablets with Raman imaging.[196] Spatially offset Raman spectroscopy (SORS) or transmission Raman spectroscopy has also been integrated into pharmaceutical studies to address the penetration depth issue at the expense of spatial resolution. The accuracy of carbamazepine polymorph and cocrystal quantification with transmission geometry notably exceeded that of the conventional backscattering modality.[197,198] A spatial offset either from a lateral displacement between the position of the collection of Raman photons and the laser irradiation spot or from sample displacement (defocusing) has provided a more in-depth analysis of solid-state form changes of multi-layer and multi-component tablets and coating thickness.[199–201] However, these studies lack spatial resolution because diffusely scattered Raman photons are collected.

Besides visualizing drug component distribution in formulations, another important application of Raman is imaging and tracking the dynamic processes of formulation stability and dissolution/solubilization over time. For example, Fateixa *et al.* used confocal RS imaging to investigate degradation mechanisms and tablet compositional changes under various storage conditions.[202] Abouselo *et al.* revealed a reliance on salt disproportionation reactions for excipient-influenced microenvironmental pH *in situ*.[203] Excipients also influence API release, which can be determined with *in vitro* dissolution profiles. Galata *et al.* utilized convolutional neural networks to evaluate chemical maps obtained through fast Raman imaging to predict dissolution profiles of sustained-release tablets.[204,205]

For dissolution monitoring and stability study, CRS imaging offers distinct advantages over spontaneous Raman owing to its high-speed imaging capability. Francis *et al.* used continuous *in situ* 3D SRS imaging to monitor the dissolution of individual entecavir particles in a long-acting implant drug formulation for treating chronic hepatitis B.[206] Figueroa *et al.* applied SRS to monitor the salt disproportionation reaction, an undesirable outcome indicating drug instability, of pioglita-zone hydrochloride (PIO-HCl) at low drug loading (1% w/w) in the presence of excipient magnesium stearate (Mgst).[207] Through a partial least squares fitting of Raman spectra spanning a spectral window of 1560–1760 cm^{-1}, they were able to accurately track the salt disproportionation reaction and revealed the role of water in mediating proton transfer between PIO-HCl and Mgst. Wei *et al.* revealed potential alterations to tablet properties by subjecting them to accelerated aging with high heat and high humidity conditions.[208] The 1350–1450 cm^{-1} and 2700–3100 cm^{-1} Raman bands were selectively sampled to target key regions informative to changes of the API, naproxen (Figure 7b.i). They observed significant modifications in the surface area and grain size of both naproxen and the crucial excipient, hydroxypropyl methylcellulose (HPMC) under stressed conditions (Figure 7b.ii).

CRS imaging has also been used to study formulations of biological drugs. Recently, Wong *et al.* applied SRS to study silicone oil-induced protein drug aggregation in subcutaneous formulations used in prefilled syringes.[209] Using hyperspectral SRS imaging in the C–H region as well as spectral phasor and nonnegative linear least squares regression analysis, the study segmented subvisible particles within a stressed therapeutic solution at a submicron resolution (Figure 7c.i.). Anodisk and polycarbonate filters were used to immobilize protein aggregates and increase the imaging throughput for compositional quantification of individual particles of varying sizes (Figure 7c.ii.). Spectral unmixing revealed that the subvisible particles in the formulation are predominantly a combination of protein and silicone oil components, challenging traditional morphological metrics that oversimplify the categorization of particles.

As more Raman imaging studies are carried out in various drug formulations, it is foreseeable that Raman will play an increasingly important role in understanding drug stability and drug bioavailability. The fast-imaging capability of SRS is particularly powerful for investigating dynamic processes of dissolution, polymorphic changes, and microscale chemical reactions with high spatiotemporal resolution. However, it is also important to recognize the inherent imaging depth limitations of Raman techniques. Although techniques like SORS and transmission Raman can still be used to measure bulk chemical composition,

the loss in spatial resolution and sensitivity in low drug loading situations will be a major challenge. A combination of Raman imaging and SORS together with other spectroscopy and imaging techniques such as micro-CT or NMR may provide a more comprehensive picture to tackle challenges in designing better pharmaceutical formulations.

Conclusion and Future Prospects

Drug discovery and development is a costly process. Despite tremendous progress in the past decade that led to many breakthroughs, particularly in targeted cancer drugs, biologics, immunotherapy, RNA-based therapies, etc., the high failure rate in translating drug candidates to FDA-approved therapeutics is still a formidable challenge. The landscape of pharmaceutical drug discovery and development is continually evolving, with current trends emphasizing targeted therapies and personalized/precision medicine. These new drug development efforts require a deep understanding of drug-target interaction at both the molecular and cellular levels in complex biological models that recapitulate many aspects of *in vivo* human conditions. Chemical imaging, particularly advanced Raman techniques, can play a pivotal role in addressing this challenge by offering unprecedented insights into the dynamic spatial distribution and metabolism of drug molecules as well as their effect on cells within complex biological matrices.

In this review, we highlighted recent developments in applying both traditional Raman and CRS techniques to study drug transport, uptake, metabolism, and effect in biological cells. Applications to drug formulations are also discussed. SRS has proved to be a powerful tool for direct imaging of small molecule drugs with or without distinct Raman peaks in the cell silent region. A prominent example is the quantitative SRS imaging of weakly basic drugs, including many kinase inhibitors that are selectively enriched in lysosomes. Imaging of other drugs is mostly limited by poor sensitivity, which is typically at the low millimolar range. The use of alkyne or nitrile Raman tag helps quantification by avoiding cellular background, but they do not significantly boost sensitivity unless large, conjugated chromophore groups are introduced, which may perturb drug uptake and function. When direct drug imaging is not possible, the metabolic or phenotypic changes of cells can be used as a proxy to determine drug response. It has been shown that *de novo* lipid or protein synthesis and fatty acid uptake are frequently perturbed under drug treatment, thus SRS imaging in the C–H region can be an effective tool for imaging single-cell drug response. An alternative approach uses deuterated metabolic substrates as tracers to probe metabolic activities directly. This method has been effective for susceptibility and efficacy testing in antibiotic, antifungal, and anticancer drugs. A significant advantage is that single-cell drug response can be measured, potentially allowing detailed studies of variability in drug resistance, and understanding its mechanism.

It is interesting to compare Raman and SRS in the context of cellular imaging. There is a convergence in maximizing the information throughput by increasing traditional Raman speed or increasing SRS spectral coverage. Both are challenging but are actively pursued. Acquiring full (or at least a broad coverage) Raman spectrum is important for detecting subtle changes that can better characterize drug metabolism or subtle metabolic changes in cells. SRS has not been able to reach the same level of spectral coverage and reproducibility

as traditional Raman. Conversely, it is unrealistic to get Raman imaging speed to match that of SRS, which is important for live cell and tissue imaging. Perhaps the best solution is to have two modalities in one instrument. Broadband CARS microscopy has been shown to provide full Raman spectral coverage through the use of supercontinuum lasers while offering milli-second or even faster spectral acquisition speed.[210–212] Although it is still much slower than SRS with narrower spectral coverage (~300 cm^{-1}), there is room for further improvement and the broad coverage may enable new studies of drugs with few distinct Raman peaks. However, it remains to be seen if such systems are compatible with live cell imaging due to the possibility of increased optical and local heating damage.

As drug discovery and development increasingly employ complex 3D tissue models such as organoids, tissue slices, and organ-on-a-chip, it is necessary to adapt Raman and CRS imaging systems for those samples. Compared to imaging 2D cell cultures, 3D model systems are advantageous because they offer a more physiologically relevant context and better recapitulate essential cell-cell and cell-matrix interactions and cell functions. However, they are also more difficult to study due to increased light scattering. Although scattering-induced intensity loss can be normalized,[161] it can restrict imaging depth and further lower the sensitivity. Nonetheless, Raman imaging has the unique advantage of label-free quantitative imaging with chemical specificity and thus is poised to play a major role in the applications of complex 3D tissue models for drug discovery. A special application area of using skin tissue for studying transdermal drug delivery has already benefited from CRS imaging of drug permeation. We expect that more applications in other tissue models in the context of drug discovery will emerge as CRS imaging and associated data analysis tools mature over the next few years.

Another underappreciated aspect of Raman imaging is its ability for long-term tracking of drug uptake or drug response. In principle, Raman is noninvasive and can follow live cells and tissues for a long time instead of as an endpoint imaging technique. However, few studies have truly achieved longitudinal live cell imaging in an appropriate cell culture environment, including temperature control, pH maintenance, and medium perfusion. CRS has additional challenges compared to traditional Raman because the coherent signal generation process means that the majority of the signal will propagate in the transmission direction and a high numerical aperture collection optics is necessary to maximize sensitivity. This constraint limits the working distance available for maintaining live cell and tissue culture, which makes most on-stage live cell culture devices incompatible or suboptimal with CRS imaging. New approaches for culture and imaging are needed to overcome this challenge in the future.

Lastly, CRS techniques have not been adopted widely in the biological or pharmaceutical research community compared to traditional Raman imaging. A major impediment is the lack of a unified platform for routine and reproducible imaging. Custom, home-brew CRS implementations are still the norm in published research articles. With the increasing commercialization of CRS systems and laser systems such as the Refined Laser Systems Picus Duo, Leica Stellaris CRS, and APE picoEmerald, improved standardization of CRS systems will happen in the near future. These developments will be critical to catalyze the

adoption of CRS in the broader biological and pharmaceutical community and potentially accelerate drug discovery and development.

ACKNOWLEDGMENT

This work was supported by the NIH R35 GM133435 to D.F. TOC figure was created with BioRender.com.

Biographies

Erin L. Dunnington Erin Dunnington received her bachelor's degree in chemistry at the University of Portland in 2021 and is currently pursuing her Ph.D. degree at the University of Washington, Seattle. Her research focuses on the development and application of quantitative stimulated Raman scattering imaging techniques for single-cell drug uptake and drug response measurements.

Brian S. Wong Brian Wong studied Biochemistry and Chemistry at the University of Washington. He received his MS in Applied Chemical Science and Technology from the University of Washington in 2022. Currently, he is a Ph.D. student at the University of Washington, working on applying and developing stimulated Raman scattering techniques to understand drug product and drug-cell interactions at the cellular scale.

Dan Fu Dr. Dan Fu is an Associate professor of Chemistry at the University of Washington, Seattle. He received his bachelor's degree from Peking University in China and Ph.D. from Princeton University under the supervision of Prof. Warren Warren. He worked with Professor Sunney Xie at Harvard University as a postdoctoral fellow, where he developed stimulated Raman scattering imaging methods. Dr. Fu joined the chemistry faculty of the University of Washington in 2015. Currently, his main research interests are the development and applications of quantitative chemical imaging tools to study various pathophysiological processes of living biological specimens at single-cell resolution.

REFERENCES

(1). Sun D; Gao W; Hu H; Zhou S Why 90% of Clinical Drug Development Fails and How to Improve It? Acta Pharm. Sin. B 2022, 12 (7), 3049–3062. 10.1016/j.apsb.2022.02.002. [PubMed: 35865092]

(2). Sinha S; Vohora D Chapter 2 - Drug Discovery and Development: An Overview. In Pharmaceutical Medicine and Translational Clinical Research; Vohora D, Singh G, Eds.; Academic Press: Boston, 2018; pp 19–32. 10.1016/B978-0-12-802103-3.00002-X.

(3). Takebe T; Imai R; Ono S The Current Status of Drug Discovery and Development as Originated in United States Academia: The Influence of Industrial and Academic Collaboration on Drug Discovery and Development. Clin. Transl. Sci 2018, 11 (6), 597–606. 10.1111/cts.12577. [PubMed: 29940695]

(4). Harrison RK Phase II and Phase III Failures: 2013–2015. Nat. Rev. Drug Discov 2016, 15 (12), 817–818. 10.1038/nrd.2016.184. [PubMed: 27811931]

(5). Moffat JG; Vincent F; Lee JA; Eder J; Prunotto M Opportunities and Challenges in Phenotypic Drug Discovery: An Industry Perspective. Nat. Rev. Drug Discov 2017, 16 (8), 531–543. 10.1038/nrd.2017.111. [PubMed: 28685762]

(6). Waring MJ; Arrowsmith J; Leach AR; Leeson PD; Mandrell S; Owen RM; Pairaudeau G; Pennie WD; Pickett SD; Wang J; Wallace O; Weir A An Analysis of the Attrition of Drug Candidates

from Four Major Pharmaceutical Companies. Nat. Rev. Drug Discov 2015, 14 (7), 475–486. 10.1038/nrd4609. [PubMed: 26091267]

(7). Hwang TJ; Carpenter D; Lauffenburger JC; Wang B; Franklin JM; Kesselheim AS Failure of Investigational Drugs in Late-Stage Clinical Development and Publication of Trial Results. JAMA Intern. Med 2016, 176 (12), 1826–1833. 10.1001/jamainternmed.2016.6008. [PubMed: 27723879]

(8). Jensen C; Teng Y Is It Time to Start Transitioning From 2D to 3D Cell Culture? Front. Mol. Biosci 2020, 7. 10.3389/fmolb.2020.00033.

(9). Langhans SA Three-Dimensional in Vitro Cell Culture Models in Drug Discovery and Drug Repositioning. Front. Pharmacol 2018, 9. 10.3389/fphar.2018.00006.

(10). Tian M; Ma Y; Lin W Fluorescent Probes for the Visualization of Cell Viability. Acc. Chem. Res 2019, 52 (8), 2147–2157. 10.1021/acs.accounts.9b00289. [PubMed: 31335119]

(11). Bray M-A; Singh S; Han H; Davis CT; Borgeson B; Hartland C; Kost-Alimova M; Gustafsdottir SM; Gibson CC; Carpenter AE Cell Painting, a High-Content Image-Based Assay for Morphological Profiling Using Multiplexed Fluorescent Dyes. Nat. Protoc 2016, 11 (9), 1757–1774. 10.1038/nprot.2016.105. [PubMed: 27560178]

(12). Hall MD; Yasgar A; Peryea T; Braisted JC; Jadhav A; Simeonov A; Coussens NP Fluorescence Polarization Assays in High-Throughput Screening and Drug Discovery: A Review. Methods Appl. Fluoresc 2016, 4 (2), 022001. 10.1088/2050-6120/4/2/022001. [PubMed: 28809163]

(13). Iv CWS; Reyes CD; López GP Microfluidic Cell Sorting: A Review of the Advances in the Separation of Cells from Debulking to Rare Cell Isolation. Lab. Chip 2015, 15 (5), 1230–1249. 10.1039/C4LC01246A. [PubMed: 25598308]

(14). Yang Q; Li J; Wang X; Peng H; Xiong H; Chen L Strategies of Molecular Imprinting-Based Fluorescence Sensors for Chemical and Biological Analysis. Biosens. Bioelectron 2018, 112, 54–71. 10.1016/j.bios.2018.04.028. [PubMed: 29698809]

(15). Kovarik ML; Allbritton NL Measuring Enzyme Activity in Single Cells. Trends Biotechnol. 2011, 29 (5), 222–230. 10.1016/j.tibtech.2011.01.003. [PubMed: 21316781]

(16). Lou Z; Li P; Han K Redox-Responsive Fluorescent Probes with Different Design Strategies. Acc. Chem. Res 2015, 48 (5), 1358–1368. 10.1021/acs.accounts.5b00009. [PubMed: 25901910]

(17). Steinegger A; Wolfbeis OS; Borisov SM Optical Sensing and Imaging of pH Values: Spectroscopies, Materials, and Applications. Chem. Rev 2020, 120 (22), 12357–12489. 10.1021/acs.chemrev.0c00451. [PubMed: 33147405]

(18). Kabir ML; Wang F; Clayton AHA Intrinsically Fluorescent Anti-Cancer Drugs. Biology 2022, 11 (8), 1135. 10.3390/biology11081135. [PubMed: 36009762]

(19). Lang W; Yuan C; Zhu L; Du S; Qian L; Ge J; Yao SQ Recent Advances in Construction of Small Molecule-Based Fluorophore-Drug Conjugates. J. Pharm. Anal 2020, 10 (5), 434–443. 10.1016/j.jpha.2020.08.006. [PubMed: 33133727]

(20). Wang Y; Cheetham AG; Angacian G; Su H; Xie L; Cui H Peptide–Drug Conjugates as Effective Pro-drug Strategies for Targeted Delivery. Adv. Drug Deliv. Rev 2017, 110–111, 112–126. 10.1016/j.addr.2016.06.015.

(21). Vernall AJ; Hill SJ; Kellam B The Evolving Small-Molecule Fluorescent-Conjugate Toolbox for Class A GPCRs. Br. J. Pharmacol 2014, 171 (5), 1073–1084. 10.1111/bph.12265. [PubMed: 23734587]

(22). Álamo P; Pallarès V; Céspedes MV; Falgàs A; Sanchez JM; Serna N; Sánchez-García L; Voltà-Duràn E; Morris GA; Sánchez-Chardi A; Casanova I; Mangues R; Vazquez E; Villaverde A; Unzueta U Fluorescent Dye Labeling Changes the Biodistribution of Tumor-Targeted Nanoparticles. Pharmaceutics 2020, 12 (11), 1004. 10.3390/pharmaceutics12111004. [PubMed: 33105866]

(23). Snipstad S; Hak S; Baghirov H; Sulheim E; Mørch Ý; Lélu S; von Haartman E; Bäck M; Nilsson KPR; Klymchenko AS; de Lange Davies C; Åslund AKO Labeling Nanoparticles: Dye Leakage and Altered Cellular Uptake. Cytom. Part J. Int. Soc. Anal. Cytol 2017, 91 (8), 760–766. 10.1002/cyto.a.22853.

(24). Freudiger CW; Min W; Saar BG; Lu S; Holtom GR; He C; Tsai JC; Kang JX; Xie XS Label-Free Biomedical Imaging with High Sensitivity by Stimulated Raman Scattering Microscopy. Science 2008, 322 (5909), 1857–1861. 10.1126/science.1165758. [PubMed: 19095943]

(25). Wang K; Zhang D; Charan K; Slipchenko MN; Wang P; Xu C; Cheng J-X Time-Lens Based Hyperspectral Stimulated Raman Scattering Imaging and Quantitative Spectral Analysis. J. Biophotonics 2013, 6 (10), 815–820. 10.1002/jbio.201300005. [PubMed: 23840041]

(26). Fu D; Zhou J; Zhu WS; Manley PW; Wang YK; Hood T; Wylie A; Xie XS Imaging the Intracellular Distribution of Tyrosine Kinase Inhibitors in Living Cells with Quantitative Hyperspectral Stimulated Raman Scattering. Nat. Chem 2014, 6 (7), 614–622. 10.1038/nchem.1961. [PubMed: 24950332]

(27). Hong W; Liao C-S; Zhao H; Younis W; Zhang Y; Seleem MN; Cheng J-X In Situ Detection of a Single Bacterium in Complex Environment by Hyper-spectral CARS Imaging. ChemistrySelect 2016, 1 (3), 513–517. 10.1002/slct.201600166.

(28). Fu D; Yang W; Xie XS Label-Free Imaging of Neurotransmitter Acetylcholine at Neuromuscular Junctions with Stimulated Raman Scattering. J. Am. Chem. Soc 2017, 139 (2), 583–586. 10.1021/jacs.6b10727. [PubMed: 28027644]

(29). Shashkova S; Leake MC Single-Molecule Fluorescence Microscopy Review: Shedding New Light on Old Problems. Biosci. Rep 2017, 37 (4), BSR20170031. 10.1042/BSR20170031. [PubMed: 28694303]

(30). Diem M; Mazur A; Lenau K; Schubert J; Bird B; Miljković M; Krafft C; Popp J Molecular Pathology via IR and Raman Spectral Imaging. J. Biophotonics 2013, 6 (11–12), 855–886. 10.1002/jbio.201300131. [PubMed: 24311233]

(31). Gurjarpadhye AA; Parekh MB; Dubnika A; Rajadas J; Inayathullah M Infrared Imaging Tools for Diagnostic Applications in Dermatology. SM J. Clin. Med. Imaging 2015, 1 (1), 1–5. [PubMed: 26691203]

(32). Prideaux B; Stoeckli M Mass Spectrometry Imaging for Drug Distribution Studies. J. Proteomics 2012, 75 (16), 4999–5013. 10.1016/j.jprot.2012.07.028. [PubMed: 22842290]

(33). H. Holbrook J; E. Kemper G; B. Hummon A Quantitative Mass Spectrometry Imaging: Therapeutics & Biomolecules. Chem. Commun 2024, 60 (16), 2137–2151. 10.1039/D3CC05988J.

(34). Rajbhandari P; Neelakantan TV; Hosny N; Stockwell BR Spatial Pharmacology Using Mass Spectrometry Imaging. Trends Pharmacol. Sci 2024, 45 (1), 67–80. 10.1016/j.tips.2023.11.003. [PubMed: 38103980]

(35). Granborg JR; Handler AM; Janfelt C Mass Spectrometry Imaging in Drug Distribution and Drug Metabolism Studies – Principles, Applications and Perspectives. TrAC Trends Anal. Chem 2022, 146, 116482. 10.1016/j.trac.2021.116482.

(36). Palonpon AF; Sodeoka M; Fujita K Molecular Imaging of Live Cells by Raman Microscopy. Curr. Opin. Chem. Biol 2013, 17 (4), 708–715. 10.1016/j.cbpa.2013.05.021. [PubMed: 23773582]

(37). Antonio KA; Schultz ZD Advances in Biomedical Raman Microscopy. Anal. Chem 2014, 86 (1), 30–46. 10.1021/ac403640f. [PubMed: 24219139]

(38). Smith GPS; McGoverin CM; Fraser SJ; Gordon KC Raman Imaging of Drug Delivery Systems. Adv. Drug Deliv. Rev 2015, 89, 21–41. 10.1016/j.addr.2015.01.005. [PubMed: 25632843]

(39). Shen Y; Hu F; Min W Raman Imaging of Small Biomolecules. Annu. Rev. Biophys 2019, 48 (1), 347–369. 10.1146/annurev-biophys-052118-115500. [PubMed: 30892920]

(40). Kuzma BA; Pence IJ; Greenfield DA; Ho A; Evans CL Visualizing and Quantifying Antimicrobial Drug Distribution in Tissue. Adv. Drug Deliv. Rev 2021, 177, 113942. 10.1016/j.addr.2021.113942. [PubMed: 34437983]

(41). El-Mashtoly SF; Gerwert K Diagnostics and Therapy Assessment Using Label-Free Raman Imaging. Anal. Chem 2022, 94 (1), 120–142. 10.1021/acs.analchem.1c04483. [PubMed: 34852454]

(42). Liu Y; Li M; Liu H; Kang C; Yu X Strategies and Progress of Raman Technologies for Cellular Uptake Analysis of the Drug Delivery Systems. Int. J. Nanomedicine 2023, 18, 6883–6900. 10.2147/IJN.S435087. [PubMed: 38026519]

(43). Orringer DA; Pandian B; Niknafs YS; Hollon TC; Boyle J; Lewis S; Garrard M; Hervey-Jumper SL; Garton HJL; Maher CO; Heth JA; Sagher O; Wilkinson DA; Snuderl M; Venneti S; Ramkissoon SH; McFadden KA; Fisher-Hubbard A; Lieberman AP; Johnson TD; Xie XS; Trautman JK; Freudiger CW; Camelo-Piragua S Rapid Intraoperative Histology of Unprocessed Surgical Specimens via Fibre-Laser-Based Stimulated Raman Scattering Microscopy. Nat. Biomed. Eng 2017, 1 (2), 0027. 10.1038/s41551-016-0027. [PubMed: 28955599]

(44). Ji M; Orringer DA; Freudiger CW; Ramkissoon S; Liu X; Lau D; Golby AJ; Norton I; Hayashi M; Agar NYR; Young GS; Spino C; Santagata S; Camelo-Piragua S; Ligon KL; Sagher O; Xie XS Rapid, Label-Free Detection of Brain Tumors with Stimulated Raman Scattering Microscopy. Sci. Transl. Med 2013, 5 (201), 201ra119–201ra119. 10.1126/scitranslmed.3005954.

(45). Fu D; Yu Y; Folick A; Currie E; Farese RV; Tsai T-H; Xie XS; Wang MC In Vivo Metabolic Fingerprinting of Neutral Lipids with Hyperspectral Stimulated Raman Scattering Microscopy. J. Am. Chem. Soc 2014, 136 (24), 8820–8828. 10.1021/ja504199s. [PubMed: 24869754]

(46). Min W; Freudiger CW; Lu S; Xie XS Coherent Nonlinear Optical Imaging: Beyond Fluorescence Microscopy. Annu. Rev. Phys. Chem 2011, 62 (1), 507–530. 10.1146/annurev.physchem.012809.103512. [PubMed: 21453061]

(47). Zhang C; Zhang D; Cheng J-X Coherent Raman Scattering Microscopy in Biology and Medicine. Annu. Rev. Biomed. Eng 2015, 17 (1), 415–445. 10.1146/annurev-bioeng-071114-040554. [PubMed: 26514285]

(48). Cheng J-X; Xie XS Vibrational Spectroscopic Imaging of Living Systems: An Emerging Platform for Biology and Medicine. Science 2015, 350 (6264). 10.1126/science.aaa8870.

(49). Krafft C; W. Schie I; Meyer T; Schmitt M; Popp J Developments in Spontaneous and Coherent Raman Scattering Microscopic Imaging for Biomedical Applications. Chem. Soc. Rev 2016, 45 (7), 1819–1849. 10.1039/C5CS00564G. [PubMed: 26497570]

(50). Zhang C; Cheng J-X Perspective: Coherent Raman Scattering Microscopy, the Future Is Bright. APL Photonics 2018, 3 (9), 090901. 10.1063/1.5040101.

(51). Li S; Li Y; Yi R; Liu L; Qu J Coherent Anti-Stokes Raman Scattering Microscopy and Its Applications. Front. Phys 2020, 8. 10.3389/fphy.2020.598420.

(52). Fung AA; Shi L Mammalian Cell and Tissue Imaging Using Raman and Coherent Raman Microscopy. WIREs Syst. Biol. Med 2020, 12 (6), e1501. 10.1002/wsbm.1501.

(53). Shi L; Fung AA; Zhou A Advances in Stimulated Raman Scattering Imaging for Tissues and Animals. Quant. Imaging Med. Surg 2021, 11 (3), 1078101–1071101. 10.21037/qims-20-712.

(54). Steven CF; Chiarparin E; Hulme AN; Brunton VG Chapter 27 - Use of SRS Microscopy for Imaging Drugs. In Stimulated Raman Scattering Microscopy; Cheng J-X, Min W, Ozeki Y, Polli D, Eds.; Elsevier, 2022; pp 403–419. 10.1016/B978-0-323-85158-9.00030-0.

(55). Zhang S; He Y; Yue S Coherent Raman Scattering Imaging of Lipid Metabolism in Cancer. J. Innov. Opt. Health Sci 2023, 16 (03), 2230015. 10.1142/S1793545822300154.

(56). Cheng J-X; Xie XS Coherent Raman Scattering Microscopy; CRC Press: Boca Raton, 2017.

(57). Heuke S; Rigneault H Coherent Stokes Raman Scattering Microscopy (CSRS). Nat. Commun 2023, 14 (1), 3337. 10.1038/s41467-023-38941-4. [PubMed: 37286641]

(58). Vartiainen EM; Rinia HA; Müller M; Bonn M Direct Extraction of Raman Line-Shapes from Congested CARS Spectra. Opt. Express 2006, 14 (8), 3622–3630. 10.1364/OE.14.003622. [PubMed: 19516509]

(59). Liu Y; Lee YJ; Cicerone MT Broadband CARS Spectral Phase Retrieval Using a Time-Domain Kramers–Kronig Transform. Opt. Lett 2009, 34 (9), 1363–1365. 10.1364/OL.34.001363. [PubMed: 19412273]

(60). Cicerone MT; Aamer KA; Lee YJ; Vartiainen E Maximum Entropy and Time-Domain Kramers–Kronig Phase Retrieval Approaches Are Functionally Equivalent for CARS Microspectroscopy. J. Raman Spectrosc 2012, 43 (5), 637–643. 10.1002/jrs.3169.

(61). Manifold B; Fu D Quantitative Stimulated Raman Scattering Microscopy: Promises and Pitfalls. Annu. Rev. Anal. Chem 2022, 15 (1), 269–289. 10.1146/annurev-anchem-061020-015110.

(62). Figueroa B; Fu W; Nguyen T; Shin K; Manifold B; Wise F; Fu D Broadband Hyperspectral Stimulated Raman Scattering Microscopy with a Parabolic Fiber Amplifier Source. Biomed. Opt. Express 2018, 9 (12), 6116–6131. 10.1364/BOE.9.006116. [PubMed: 31065417]

(63). Figueroa B; Hu R; Rayner SG; Zheng Y; Fu D Real-Time Microscale Temperature Imaging by Stimulated Raman Scattering. J. Phys. Chem. Lett 2020, 11 (17), 7083–7089. 10.1021/acs.jpclett.0c02029. [PubMed: 32786960]

(64). Wilson LT; Tipping WJ; Wetherill C; Henley Z; Faulds K; Graham D; Mackay SP; Tomkinson NCO Mitokyne: A Ratiometric Raman Probe for Mitochondrial pH. Anal. Chem 2021, 93 (37), 12786–12792. 10.1021/acs.analchem.1c03075. [PubMed: 34505518]

(65). Murphy N; Tipping WJ; Braddick HJ; Wilson LT; Tomkinson NCO; Faulds K; Graham D; Farràs P Expanding the Range of Bioorthogonal Tags for Multiplex Stimulated Raman Scattering Microscopy. Angew. Chem. Int. Ed 2023, 62 (48), e202311530. 10.1002/anie.202311530.

(66). Chen C; Zhao Z; Qian N; Wei S; Hu F; Min W Multiplexed Live-Cell Profiling with Raman Probes. Nat. Commun 2021, 12 (1), 3405. 10.1038/s41467-021-23700-0. [PubMed: 34099708]

(67). Wei L; Chen Z; Shi L; Long R; Anzalone AV; Zhang L; Hu F; Yuste R; Cornish VW; Min W Super-Multiplex Vibrational Imaging. Nature 2017, 544 (7651), 465–470. 10.1038/nature22051. [PubMed: 28424513]

(68). Hu F; Zeng C; Long R; Miao Y; Wei L; Xu Q; Min W Supermultiplexed Optical Imaging and Barcoding with Engineered Polyynes. Nat. Methods 2018, 15 (3), 194–200. 10.1038/nmeth.4578. [PubMed: 29334378]

(69). Zhu Y; Ge X; Ni H; Yin J; Lin H; Wang L; Tan Y; Prabhu Dessai CV; Li Y; Teng X; Cheng J-X Stimulated Raman Photothermal Microscopy toward Ultrasensitive Chemical Imaging. Sci. Adv 2023, 9 (43), eadi2181. 10.1126/sciadv.adi2181. [PubMed: 37889965]

(70). El-Mashtoly SF; Petersen D; Yosef HK; Mosig A; Reinacher-Schick A; Kötting C; Gerwert K Label-Free Imaging of Drug Distribution and Metabolism in Colon Cancer Cells by Raman Microscopy. Analyst 2014, 139 (5), 1155–1161. 10.1039/C3AN01993D. [PubMed: 24427772]

(71). Aljakouch K; Lechtonen T; Yosef HK; Hammoud MK; Alsaidi W; Kötting C; Mügge C; Kourist R; El-Mashtoly SF; Gerwert K Raman Microspectroscopic Evidence for the Metabolism of a Tyrosine Kinase Inhibitor, Neratinib, in Cancer Cells. Angew. Chem. Int. Ed 2018, 57 (24), 7250–7254. 10.1002/anie.201803394.

(72). LaLone V; Mourão MA; Standiford TJ; Raghavendran K; Shedden K; Stringer KA; Rosania GR An Expandable Mechanopharmaceutical Device (3): A Versatile Raman Spectral Cytometry Approach to Study the Drug Cargo Capacity of Individual Macrophages. Pharm. Res 2018, 36 (1), 2. 10.1007/s11095-018-2540-0. [PubMed: 30402713]

(73). Koga K; Kajimoto S; Yoshizaki Y; Takahashi H; Kageyama L; Konno T; Nakabayashi T Establishment of a Method for the Introduction of Poorly Water-Soluble Drugs in Cells and Evaluation of Intracellular Concentration Distribution Using Resonance Raman Imaging. J. Phys. Chem. B 2024, 128 (6), 1350–1359. 10.1021/acs.jpcb.3c06601. [PubMed: 38295808]

(74). Sepp K; Lee M; Bluntzer MTJ; Helgason GV; Hulme AN; Brunton VG Utilizing Stimulated Raman Scattering Microscopy To Study Intracellular Distribution of Label-Free Ponatinib in Live Cells. J. Med. Chem 2020, 63 (5), 2028–2034. 10.1021/acs.jmedchem.9b01546. [PubMed: 31829628]

(75). J. Tipping W; S. Merchant A; Fearon R; O. Tomkinson NC; Faulds K; Graham D Temporal Imaging of Drug Dynamics in Live Cells Using Stimulated Raman Scattering Microscopy and a Perfusion Cell Culture System. RSC Chem. Biol 2022, 3 (9), 1154–1164. 10.1039/D2CB00160H. [PubMed: 36128503]

(76). De Duve C; De Barsy T; Poole B; Trouet A; Tulkens P; Van Hoof F Lysosomotropic Agents. Biochem. Pharmacol 1974, 23 (18), 2495–2531. 10.1016/0006-2952(74)90174-9. [PubMed: 4606365]

(77). Zhitomirsky B; Assaraf YG Lysosomes as Mediators of Drug Resistance in Cancer. Drug Resist. Updat 2016, 24, 23–33. 10.1016/j.drup.2015.11.004. [PubMed: 26830313]

(78). Gaschler MM; Hu F; Feng H; Linkermann A; Min W; Stockwell BR Determination of the Subcellular Localization and Mechanism of Action of Ferro-statins in Suppressing Ferroptosis. ACS Chem. Biol 2018, 13 (4), 1013–1020. 10.1021/acschembio.8b00199. [PubMed: 29512999]

(79). Yang J; Griffin A; Qiang Z; Ren J Organelle-Targeted Therapies: A Comprehensive Review on System Design for Enabling Precision Oncology. Signal Transduct. Target. Ther 2022, 7 (1), 1–27. 10.1038/s41392-022-01243-0. [PubMed: 34980881]

(80). Saminathan A; Zajac M; Anees P; Krishnan Y Organelle-Level Precision with next-Generation Targeting Technologies. Nat. Rev. Mater 2022, 7 (5), 355–371. 10.1038/s41578-021-00396-8.

(81). Yamakoshi H; Dodo K; Palonpon A; Ando J; Fujita K; Kawata S; Sodeoka M Alkyne-Tag Raman Imaging for Visualization of Mobile Small Molecules in Live Cells. J. Am. Chem. Soc 2012, 134 (51), 20681–20689. 10.1021/ja308529n. [PubMed: 23198907]

(82). Bae K; Zheng W; Ma Y; Huang Z Real-Time Monitoring of Pharmacokinetics of Mitochondria-Targeting Molecules in Live Cells with Bioorthogonal Hyperspectral Stimulated Raman Scattering Microscopy. Anal. Chem 2020, 92 (1), 740–748. 10.1021/acs.analchem.9b02838. [PubMed: 31750649]

(83). Yuan Y; Olawode EO; Tumey LN; Lu F Visualizing Drug-Induced Lipid Accumulation in Lysosomes of Live Cancer Cells with Stimulated Raman Imaging. Biomed. Opt. Express 2023, 14 (6), 2551–2564. 10.1364/BOE.487527. [PubMed: 37342714]

(84). Wei L; Hu F; Chen Z; Shen Y; Zhang L; Min W Live-Cell Bioorthogonal Chemical Imaging: Stimulated Raman Scattering Microscopy of Vibrational Probes. Acc. Chem. Res 2016, 49 (8), 1494–1502. 10.1021/acs.accounts.6b00210. [PubMed: 27486796]

(85). Oda R; Shou J; Zhong W; Ozeki Y; Yasui M; Nuriya M Direct Visualization of General Anesthetic Propofol on Neurons by Stimulated Raman Scattering Microscopy. iScience 2022, 25 (3), 103936. 10.1016/j.isci.2022.103936. [PubMed: 35252821]

(86). Zhong W; Oda R; Ozeki Y; Yasui M; Nuriya M Protocol to Image Deuterated Propofol in Living Rat Neurons Using Multimodal Stimulated Raman Scattering Microscopy. STAR Protoc. 2023, 4 (2), 102221. 10.1016/j.xpro.2023.102221. [PubMed: 37060560]

(87). Dong P-T; Zong C; Dagher Z; Hui J; Li J; Zhan Y; Zhang M; Mansour MK; Cheng J-X Polarization-Sensitive Stimulated Raman Scattering Imaging Resolves Amphotericin B Orientation in *Candida* Membrane. Sci. Adv 2021, 7 (2), eabd5230. 10.1126/sciadv.abd5230. [PubMed: 33523971]

(88). Wong BS; Dunnington EL; Wu R; Kim JI; Hu K; Ro TH; Fu D Facilitated Transport of EGFR Inhibitors Plays an Important Role in Their Cellular Uptake. Anal. Chem 2024, 96 (4), 1547–1555. 10.1021/acs.analchem.3c04242. [PubMed: 38214696]

(89). Matousek P Deep Non-Invasive Raman Spectroscopy of Living Tissue and Powders. Chem. Soc. Rev 2007, 36 (8), 1292–1304. 10.1039/B614777C. [PubMed: 17619689]

(90). Ashtikar M; Matthäus C; Schmitt M; Krafft C; Fahr A; Popp J Non-Invasive Depth Profile Imaging of the Stratum Corneum Using Confocal Raman Microscopy: First Insights into the Method. Eur. J. Pharm. Sci 2013, 50 (5), 601–608. 10.1016/j.ejps.2013.05.030. [PubMed: 23764946]

(91). Hill AH; Manifold B; Fu D Tissue Imaging Depth Limit of Stimulated Raman Scattering Microscopy. Biomed. Opt. Express 2020, 11 (2), 762–774. 10.1364/BOE.382396. [PubMed: 32133223]

(92). Francis AT; Manifold B; Carlson EC; Hu R; Hill AH; Men S; Fu D In Vivo Simultaneous Nonlinear Absorption Raman and Fluorescence (SNARF) Imaging of Mouse Brain Cortical Structures. Commun. Biol 2022, 5 (1), 1–8. 10.1038/s42003-022-03166-6. [PubMed: 34987157]

(93). Wei M; Shi L; Shen Y; Zhao Z; Guzman A; Kaufman LJ; Wei L; Min W Volumetric Chemical Imaging by Clearing-Enhanced Stimulated Raman Scattering Microscopy. Proc. Natl. Acad. Sci 2019, 116 (14), 6608–6617. 10.1073/pnas.1813044116. [PubMed: 30872474]

(94). Woodhouse N; Majer J; Marshall P; Hood S; Not-ingher I Quantification of Drugs in Brain and Liver Mimetic Tissue Models Using Raman Spectroscopy. Appl. Spectrosc 2023, 77 (3), 246–260. 10.1177/00037028221139494. [PubMed: 36320126]

(95). Sperati CJ; Zhang C; Delsante M; Gupta R; Bagnasco S; Barman I Raman Spectroscopy for the Diagnosis of Intratubular Triamterene Crystallization. Kidney Int. Rep 2018, 3 (4), 997–1003. 10.1016/j.ekir.2018.03.010. [PubMed: 29989004]

(96). Spencer-Dene B; Mukherjee P; Alex A; Bera K; Tseng W-J; Shi J; Chaney EJ; Spillman DR; Marjanovic M; Miranda E; Boppart SA; Hood SR Localization of Unlabeled Bepirovirsen Antisense Oligonucleotide in Murine Tissues Using in Situ Hybridization and CARS Imaging. RNA 2023, 29 (10), 1575–1590. 10.1261/rna.079699.123. [PubMed: 37460153]

(97). Tapfumaneyi P; Imran M; Mohammed Y; Roberts MS Recent Advances and Future Prospective of Topical and Transdermal Delivery Systems. Front. Drug Deliv 2022, 2. 10.3389/fddev.2022.957732.

(98). Supe S; Takudage P Methods for Evaluating Penetration of Drug into the Skin: A Review. Skin Res. Technol 2021, 27 (3), 299–308. 10.1111/srt.12968. [PubMed: 33095948]

(99). Zsikó S; Csányi E; Kovács A; Budai-Szűcs M; Gácsi A; Berkó S Methods to Evaluate Skin Penetration In Vitro. Sci. Pharm 2019, 87 (3), 19. 10.3390/scipharm87030019.

(100). Jung N; Namjoshi S; Mohammed Y; Grice JE; Benson HAE; Raney SG; Roberts MS; Wind-bergs M Application of Confocal Raman Microscopy for the Characterization of Topical Semisolid Formulations and Their Penetration into Human Skin Ex Vivo. Pharm. Res 2022, 39 (5), 935–948. 10.1007/s11095-022-03245-7. [PubMed: 35411509]

(101). Iermak I; da Silva AP; Kurachi C; Bagnato VS; Inada NM Raman Microspectroscopy as a Tool to Elucidate the Efficacy of Topical Formulations Containing Curcumin. Pharmaceuticals 2019, 12 (1), 44. 10.3390/ph12010044. [PubMed: 30909531]

(102). Zhang Q; Flach CR; Mendelsohn R; Page L; Whitson S; Boncheva Bettex M Visualization of Epidermal Reservoir Formation from Topical Diclofenac Gels by Raman Spectroscopy. J. Pain Res 2020, 13, 1621–1627. 10.2147/JPR.S253069. [PubMed: 32753939]

(103). Krombholz R; Liu Y; Lunter DJ In-Line and Off-Line Monitoring of Skin Penetration Profiles Using Confocal Raman Spectroscopy. Pharmaceutics 2021, 13 (1), 67. 10.3390/pharmaceutics13010067. [PubMed: 33430237]

(104). Garvie-Cook H; Hoppel M; Guy RH Raman Spectroscopic Tools to Probe the Skin–(Trans)Dermal Formulation Interface. Mol. Pharm 2022, 19 (11), 4010–4016. 10.1021/acs.molpharmaceut.2c00480. [PubMed: 36066005]

(105). Xu T; Yilmaz H; Willett DR; Strasinger C; Rodriguez JD; Keire DA; Wokovich AM Raman Mapping of Fentanyl Transdermal Delivery Systems with Off-Label Modifications. Analyst 2020, 145 (3), 953–962. 10.1039/C9AN01289C. [PubMed: 31825408]

(106). Zarmpi P; Tabosa MAM; Vitry P; Bunge AL; Belsey NA; Tsikritsis D; Woodman TJ; Delgado-Charro MB; Guy RH Confocal Raman Spectroscopic Characterization of Dermatopharmacokinetics Ex Vivo. Mol. Pharm 2023, 20 (11), 5910–5920. 10.1021/acs.molpharmaceut.3c00755. [PubMed: 37801410]

(107). Goel A; Tsikritsis D; Belsey NA; Pendlington R; Glavin S; Chen T Measurement of Chemical Penetration in Skin Using Stimulated Raman Scattering Microscopy and Multivariate Curve Resolution - Alternating Least Squares. Spectrochim. Acta. A. Mol. Biomol. Spectrosc 2023, 296, 122639. 10.1016/j.saa.2023.122639. [PubMed: 36989692]

(108). Maciel Tabosa MA; Vitry P; Zarmpi P; Bunge AL; Belsey NA; Tsikritsis D; Woodman TJ; White KAJ; Delgado-Charro MB; Guy RH Quantification of Chemical Uptake into the Skin by Vibrational Spectroscopies and Stratum Corneum Sampling. Mol. Pharm 2023, 20 (5), 2527–2535. 10.1021/acs.molpharmaceut.2c01109. [PubMed: 37053523]

(109). Zarmpi P; Tsikritsis D; Vorng J-L; Belsey NA; Bunge AL; Woodman TJ; Delgado-Charro MB; Guy RH Evaluation of Chemical Disposition in Skin by Stimulated Raman Scattering Microscopy. J. Controlled Release 2024, S0168–3659(24)00098–1. 10.1016/j.jconrel.2024.02.011.

(110). Sarri B; Chen X; Canonge R; Grégoire S; Formanek F; Galey J-B; Potter A; Bornschlögl T; Rigneault H In Vivo Quantitative Molecular Absorption of Glycerol in Human Skin Using Coherent Anti-Stokes Raman Scattering (CARS) and Two-Photon Auto-Fluorescence. J. Controlled Release 2019, 308, 190–196. 10.1016/j.jconrel.2019.07.018.

(111). Ito T; Iguchi R; Matsuoka F; Nishi Y; Ogihara T; Misawa K Label-Free Skin Penetration Analysis Using Time-Resolved, Phase-Modulated Stimulated Raman Scattering Microscopy. Biomed. Opt. Express 2021, 12 (10), 6545. 10.1364/BOE.436142. [PubMed: 34745755]

(112). Feizpour A; Marstrand T; Bastholm L; Eirefelt S; Evans CL Label-Free Quantification of Pharmacokinetics in Skin with Stimulated Raman Scattering Microscopy and Deep Learning. J. Invest. Dermatol 2021, 141 (2), 395–403. 10.1016/j.jid.2020.06.027. [PubMed: 32710899]

(113). Kuzma BA; Tu D; Goss A; Iliopoulos F; Slade JB; Wiatrowski A; Feizpour A; Evans CL Instantaneous Topical Drug Quantification Using a 3D Printed Microfluidic Device and Coherent Raman Imaging. OpenNano 2023, 12, 100151. 10.1016/j.onano.2023.100151.

(114). Iliopoulos F; Tu D; Pence IJ; Li X; Ghosh P; Luke MC; Raney SG; Rantou E; Evans CL Determining Topical Product Bioequivalence with Stimulated Raman Scattering Microscopy. J. Controlled Release 2024, 367, 864–876. 10.1016/j.jconrel.2024.02.010.

(115). Wanjiku B; Yamamoto K; Klossek A; Schumacher F; Pischon H; Mundhenk L; Rancan F; Judd MM; Ahmed M; Zoschke C; Kleuser B; Rühl E; Schäfer-Korting M Qualifying X-Ray and Stimulated Raman Spectromicroscopy for Mapping Cutaneous Drug Penetration. Anal. Chem 2019, 91 (11), 7208–7214. 10.1021/acs.analchem.9b00519. [PubMed: 31090401]

(116). Belsey NA; Dexter A; Vorng J-L; Tsikritsis D; Nikula CJ; Murta T; Tiddia M-V; Zhang J; Gurdak E; Trindade GF; Gilmore IS; Page L; Roper CS; Guy RH; Bettex MB Visualisation of Drug Distribution in Skin Using Correlative Optical Spectroscopy and Mass Spectrometry Imaging. J. Controlled Release 2023, 364, 79–89. 10.1016/j.jconrel.2023.10.026.

(117). Patel T; Zhou J; Piepmeier JM; Saltzman WM Polymeric Nanoparticles for Drug Delivery to the Central Nervous System. Adv. Drug Deliv. Rev 2012, 64 (7), 701–705. 10.1016/j.addr.2011.12.006. [PubMed: 22210134]

(118). Hossen S; Hossain MK; Basher MK; Mia MNH; Rahman MT; Uddin MJ Smart Nanocarrier-Based Drug Delivery Systems for Cancer Therapy and Toxicity Studies: A Review. J. Adv. Res 2019, 15, 1–18. 10.1016/j.jare.2018.06.005. [PubMed: 30581608]

(119). Liu P; Chen G; Zhang J A Review of Liposomes as a Drug Delivery System: Current Status of Approved Products, Regulatory Environments, and Future Perspectives. Molecules 2022, 27 (4), 1372. 10.3390/molecules27041372. [PubMed: 35209162]

(120). Wilson B; Geetha KM Lipid Nanoparticles in the Development of mRNA Vaccines for COVID-19. J. Drug Deliv. Sci. Technol 2022, 74, 103553. 10.1016/j.jddst.2022.103553. [PubMed: 35783677]

(121). Saunders C; de Villiers CA; Stevens MM Single Particle Chemical Characterisation of Nanoformulations for Cargo Delivery. AAPS J. 2023, 25 (6), 94. 10.1208/s12248-023-00855-w. [PubMed: 37783923]

(122). Klemm P; Solomun JI; Rodewald M; Kuchenbrod MT; Hänsch VG; Richter F; Popp J; Hertweck C; Hoeppener S; Bonduelle C; Lecommandoux S; Traeger A; Schubert S Efficient Gene Delivery of Tailored Amphiphilic Polypeptides by Polyplex Surfing. Biomacromolecules 2022, 23 (11), 4718–4733. 10.1021/acs.biomac.2c00919. [PubMed: 36269943]

(123). Foo W; Cseresnyés Z; Rössel C; Teng Y; Ramoji A; Chi M; Hauswald W; Huschke S; Hoeppener S; Popp J; Schacher FH; Sierka M; Figge MT; Press AT; Bauer M Tuning the Corona-Core Ratio of Polyplex Micelles for Selective Oligonucleotide Delivery to Hepatocytes or Hepatic Immune Cells. Biomaterials 2023, 294, 122016. 10.1016/j.biomaterials.2023.122016. [PubMed: 36702000]

(124). Kreofsky NW; Roy P; Brown ME; Perez U; Leighton RE; Frontiera RR; Reineke TM Cinchona Alkaloid Polymers Demonstrate Highly Efficient Gene Delivery Dependent on Stereochemistry, Methoxy Substitution, and Length. Biomacromolecules 2024, 25 (1), 486–501. 10.1021/acs.biomac.3c01099. [PubMed: 38150323]

(125). Penders J; Pence IJ; Horgan CC; Bergholt MS; Wood CS; Najer A; Kauscher U; Nagelkerke A; Stevens MM Single Particle Automated Raman Trapping Analysis. Nat. Commun 2018, 9 (1), 4256. 10.1038/s41467-018-06397-6. [PubMed: 30323298]

(126). Potter M; Najer A; Klöckner A; Zhang S; Holme MN; Nele V; Che J; Massi L; Penders J; Saunders C; Doutch JJ; Edwards AM; Ces O; Stevens MM Controlled Dendrimersome Nanoreactor System for Localized Hypochlorite-Induced Killing of Bacteria. ACS Nano 2020, 14 (12), 17333–17353. 10.1021/acsnano.0c07459. [PubMed: 33290039]

(127). Barriga HMG; Pence IJ; Holme MN; Doutch JJ; Penders J; Nele V; Thomas MR; Carroni M; Stevens MM Coupling Lipid Nanoparticle Structure and Automated Single-Particle Composition Analysis to Design Phospholipase-Responsive Nanocarriers. Adv. Mater 2022, 34 (26), 2200839. 10.1002/adma.202200839.

(128). Najer A; Kim J; Saunders C; Che J; Baum J; Stevens MM Enhanced Antimalarial and Antisequestration Activity of Methoxybenzenesulfonate-Modified Biopolymers and

Nanoparticles for Tackling Severe Malaria. ACS Infect. Dis 2024, 10 (2), 732–745. 10.1021/acsinfecdis.3c00564. [PubMed: 38271991]

(129). Saunders C; Foote JEJ; Wojciechowski JP; Cammack A; Pedersen SV; Doutch JJ; Barriga HMG; Holme MN; Penders J; Chami M; Najer A; Stevens MM Revealing Population Heterogeneity in Vesicle-Based Nanomedicines Using Automated, Single Particle Raman Analysis. ACS Nano 2023, 17 (12), 11713–11728. 10.1021/acsnano.3c02452. [PubMed: 37279338]

(130). Godfrey L; Iannitelli A; Garrett NL; Moger J; Imbert I; King T; Porreca F; Soundararajan R; Lalatsa A; Schätzlein AG; Uchegbu IF Nanoparticulate Peptide Delivery Exclusively to the Brain Produces Tolerance Free Analgesia. J. Controlled Release 2018, 270, 135–144. 10.1016/j.jconrel.2017.11.041.

(131). Bera K; Rojas-Gómez RA; Mukherjee P; Snyder CE; Aksamitiene E; Alex A; Spillman DR; Marjanovic M; Shabana A; Johnson R; Hood SR; Boppart SA Probing Delivery of a Lipid Nanoparticle Encapsulated Self-Amplifying mRNA Vaccine Using Coherent Raman Microscopy and Multiphoton Imaging. Sci. Rep 2024, 14 (1), 4348. 10.1038/s41598-024-54697-3. [PubMed: 38388635]

(132). Vanden-Hehir S; Cairns SA; Lee M; Zoupi L; Shaver MP; Brunton VG; Williams A; Hulme AN Alkyne-Tagged PLGA Allows Direct Visualization of Nanoparticles In Vitro and Ex Vivo by Stimulated Raman Scattering Microscopy. Biomacromolecules 2019, 20 (10), 4008–4014. 10.1021/acs.biomac.9b01092. [PubMed: 31408325]

(133). Gao X; Lang X; El Khoury E; Wei M; Qian N; Min W Quantitative Label-Free Chemical Imaging of PLGA Nanoparticles in Cells and Tissues with Single-Particle Sensitivity. Nano Lett. 2024, 24 (3), 1024 10.1021/acs.nanolett.3c04463. [PubMed: 38207237]

(134). Wei M; Qian N; Gao X; Lang X; Song D; Min W Single-Particle Imaging of Nanomedicine Entering the Brain. Proc. Natl. Acad. Sci 2024, 121 (5), e2309811121. 10.1073/pnas.2309811121. [PubMed: 38252832]

(135). Afseth NK; Segtnan VH; Wold JP Raman Spectra of Biological Samples: A Study of Preprocessing Methods. Appl. Spectrosc 2006, 60 (12), 1358–1367. [PubMed: 17217584]

(136). Cutshaw G; Hassan N; Uthaman S; Wen X; Singh B; Sarkar A; Bardhan R Monitoring Metabolic Changes in Response to Chemotherapies in Cancer with Raman Spectroscopy and Metabolomics. Anal. Chem 2023, 95 (35), 13172–13184. 10.1021/acs.analchem.3c02073. [PubMed: 37605298]

(137). S. Mondol A; F. El-Mashtoly S; Frick T; Gerwert K; Popp J; W. Schie I High-Content Screening Raman Spectroscopy (HCS-RS) of Panitumumab-Exposed Colorectal Cancer Cells. Analyst 2019, 144 (20), 6098–6107. 10.1039/C9AN01176E. [PubMed: 31531499]

(138). Deng X; Milligan K; Brolo A; Lum JJ; Andrews JL; Jirasek A Radiation Treatment Response and Hypoxia Biomarkers Revealed by Machine Learning Assisted Raman Spectroscopy in Tumour Cells and Xenograft Tissues. Analyst 2022, 147 (22), 5091–5104. 10.1039/D2AN01222G. [PubMed: 36217911]

(139). Kanmalar M; Abdul Sani SF; Kamri NINB; Said NABM; Jamil AHBA; Kuppusamy S; Mun KS; Bradley DA Raman Spectroscopy Biochemical Characterisation of Bladder Cancer Cisplatin Resistance Regulated by FDFT1: A Review. Cell. Mol. Biol. Lett 2022, 27 (1), 9. 10.1186/s11658-022-00307-x. [PubMed: 35093030]

(140). Wen X; Ou Y-C; Bogatcheva G; Thomas G; Mahadevan-Jansen A; Singh B; C. Lin E; Bardhan R Probing Metabolic Alterations in Breast Cancer in Response to Molecular Inhibitors with Raman Spectroscopy and Validated with Mass Spectrometry. Chem. Sci 2020, 11 (36), 9863–9874. 10.1039/D0SC02221G. [PubMed: 34094246]

(141). Wang H; Li J; Qin J; Li J; Chen Y; Song D; Zeng H; Wang S Confocal Raman Microspectral Analysis and Imaging of the Drug Response of Osteosarcoma to Cisplatin. Anal. Methods 2021, 13 (22), 2527–2536. 10.1039/D1AY00626F. [PubMed: 34008598]

(142). Wang H; Li J; Qin J; Li J; Chen Y; Song D; Zeng H; Wang S Investigating the Cellular Responses of Osteosarcoma to Cisplatin by Confocal Raman Microspectroscopy. J. Photochem. Photobiol. B 2022, 226, 112366. 10.1016/j.jphotobiol.2021.112366. [PubMed: 34826719]

(143). E. Jamieson L; Wetherill C; Faulds K; Graham D Ratiometric Raman Imaging Reveals the New Anti-Cancer Potential of Lipid Targeting Drugs. Chem. Sci 2018, 9 (34), 6935–6943. 10.1039/C8SC02312C. [PubMed: 30258563]

(144). Zhang Y; Xu J; Yu Y; Shang W; Ye A Anti-Cancer Drug Sensitivity Assay with Quantitative Heterogeneity Testing Using Single-Cell Raman Spectroscopy. Molecules 2018, 23 (11), 2903. 10.3390/molecules23112903. [PubMed: 30405051]

(145). Larion M; Dowdy T; Ruiz-Rodado V; Meyer MW; Song H; Zhang W; Davis D; Gilbert MR; Lita A Detection of Metabolic Changes Induced via Drug Treatments in Live Cancer Cells and Tissue Using Raman Imaging Microscopy. Biosensors 2019, 9 (1), 5. 10.3390/bios9010005.

(146). Hammoud MK; Yosef HK; Lechtonen T; Aljakouch K; Schuler M; Alsaidi W; Daho I; Maghnouj A; Hahn S; El-Mashtoly SF; Gerwert K Raman Micro-Spectroscopy Monitors Acquired Resistance to Targeted Cancer Therapy at the Cellular Level. Sci. Rep 2018, 8 (1), 15278. 10.1038/s41598-018-33682-7. [PubMed: 30323297]

(147). Schuler I; Schuler M; Frick T; Jimenez D; Maghnouj A; Hahn S; Zewail R; Gerwert K; F. El-Mashtoly S Efficacy of Tyrosine Kinase Inhibitors Examined by a Combination of Raman Micro-Spectroscopy and a Deep Wavelet Scattering-Based Multivariate Analysis Framework. Analyst 2024. 10.1039/D3AN02235H.

(148). Yay A; Onses MS; Sahmetlioglu E; Ceyhan A; Pekdemir S; Onder GO; Sezer G; Sarica ZS; Aydin F Raman Spectroscopy: A Novel Experimental Approach to Evaluating Cisplatin Induced Tissue Damage. Talanta 2020, 207, 120343. 10.1016/j.talanta.2019.120343. [PubMed: 31594623]

(149). Cao H; Ma C; Wu Z; Sun L; Liu W; Ma C; Chen F; Peng Z; Xuan L; Huang R; Pan G Label-Free Raman Spectroscopy for the Assessment of Liver Fibrosis. MedComm – Future Med. 2023, 2 (4), e68. 10.1002/mef2.68.

(150). Li M; Liao H-X; Bando K; Nawa Y; Fujita S; Fujita K Label-Free Monitoring of Drug-Induced Cytotoxicity and Its Molecular Fingerprint by Live-Cell Raman and Autofluorescence Imaging. Anal. Chem 2022. 10.1021/acs.analchem.2c00293.

(151). LaLone V; Fawaz MV; Morales-Mercado J; Mourão MA; Snyder CS; Kim SY; Lieberman AP; Tuteja A; Mehta G; Standiford TJ; Raghavendran K; Shedden K; Schwendeman A; Stringer KA; Rosania GR Inkjet-Printed Micro-Calibration Standards for Ultraquantitative Raman Spectral Cytometry. Analyst 2019, 144 (12), 3790–3799. 10.1039/C9AN00500E. [PubMed: 31116195]

(152). LaLone V; Aizenshtadt A; Goertz J; Skottvoll FS; Mota MB; You J; Zhao X; Berg HE; Stokowiec J; Yu M; Schwendeman A; Scholz H; Wilson SR; Krauss S; Stevens MM Quantitative Chemometric Phenotyping of Three-Dimensional Liver Organoids by Raman Spectral Imaging. Cell Rep. Methods 2023, 3 (4), 100440. 10.1016/j.crmeth.2023.100440. [PubMed: 37159662]

(153). Kawagoe H; Ando J; Asanuma M; Dodo K; Miyano T; Ueda H; Sodeoka M; Fujita K Multiwell Raman Plate Reader for High-Throughput Biochemical Screening. Sci. Rep 2021, 11 (1), 15742. 10.1038/s41598-021-95139-8. [PubMed: 34344945]

(154). Liao H-X; Bando K; Li M; Fujita K Multifocal Raman Spectrophotometer for Examining Drug-Induced and Chemical-Induced Cellular Changes in 3D Cell Spheroids. Anal. Chem 2023, 95 (39), 14616–14623. 10.1021/acs.analchem.3c02129. [PubMed: 37725051]

(155). Masia F; Pope I; Watson P; Langbein W; Borri P Bessel-Beam Hyperspectral CARS Microscopy with Sparse Sampling: Enabling High-Content High-Throughput Label-Free Quantitative Chemical Imaging. Anal. Chem 2018, 90 (6), 3775–3785. 10.1021/acs.analchem.7b04039. [PubMed: 29505230]

(156). J. Tipping W; T. Wilson L; An C; A. Leventi A; W. Wark A; Wetherill C; O. Tomkinson NC; Faulds K; Graham D Stimulated Raman Scattering Microscopy with Spectral Phasor Analysis: Applications in Assessing Drug–Cell Interactions. Chem. Sci 2022, 13 (12), 3468–3476. 10.1039/D1SC06976D. [PubMed: 35432863]

(157). Hislop EW; Tipping WJ; Faulds K; Graham D Label-Free Imaging of Lipid Droplets in Prostate Cells Using Stimulated Raman Scattering Microscopy and Multivariate Analysis. Anal. Chem 2022, 94 (25), 8899–8908. 10.1021/acs.analchem.2c00236. [PubMed: 35699644]

(158). Baek S; Nah S; Park JY; Lee SJ; Kang YG; Kwon SH; Oh SJ; Lee KP; Moon BS A Novel Chalcone Derivative Exerts Anticancer Effects by Promoting Apoptotic Cell Death of Human

Pancreatic Cancer Cells. Bioorg. Med. Chem 2023, 93, 117458. 10.1016/j.bmc.2023.117458. [PubMed: 37634418]

(159). Zhang M; Dong P-T; Eldesouky HE; Zhan Y; Lin H; Wang Z; Salama EA; Jusuf S; Zong C; Chen Z; Seleem MN; Cheng J-X Fingerprint Stimulated Raman Scattering Imaging Unveils Ergosteryl Ester as a Metabolic Signature of Azole-Resistant Candida Albicans. Anal. Chem 2023, 95 (26), 9901–9913. 10.1021/acs.analchem.3c00900. [PubMed: 37310727]

(160). Shi J; Bera K; Mukherjee P; Alex A; Chaney EJ; Spencer-Dene B; Majer J; Marjanovic M; Spillman DRJ; Hood SR; Boppart SA Weakly Supervised Identification and Localization of Drug Fingerprints Based on Label-Free Hyperspectral CARS Microscopy. Anal. Chem 2023, 95 (29), 10957–10965. 10.1021/acs.analchem.3c00979. [PubMed: 37450658]

(161). Oh S; Lee C; Yang W; Li A; Mukherjee A; Basan M; Ran C; Yin W; Tabin CJ; Fu D; Xie XS; Kirschner MW Protein and Lipid Mass Concentration Measurement in Tissues by Stimulated Raman Scattering Microscopy. Proc. Natl. Acad. Sci 2022, 119 (17), e2117938119. 10.1073/pnas.2117938119. [PubMed: 35452314]

(162). Bresci A; Kim JH; Ghislanzoni S; Manetti F; Wu L; Vernuccio F; Ceconello C; Sorrentino S; Barman I; Bongarzone I; Cerullo G; Vanna R; Polli D Noninvasive Morpho-Molecular Imaging Reveals Early Therapy-Induced Senescence in Human Cancer Cells. Sci. Adv 2023, 9 (37), eadg6231. 10.1126/sciadv.adg6231. [PubMed: 37703362]

(163). Wei L; Yu Y; Shen Y; Wang MC; Min W Vibrational Imaging of Newly Synthesized Proteins in Live Cells by Stimulated Raman Scattering Microscopy. Proc. Natl. Acad. Sci 2013, 110 (28), 11226–11231. 10.1073/pnas.1303768110. [PubMed: 23798434]

(164). Azemtsop Matanfack G; Rüger J; Stiebing C; Schmitt M; Popp J Imaging the Invisible—Bioorthogonal Raman Probes for Imaging of Cells and Tissues. J. Biophotonics 2020, 13 (9), e202000129. 10.1002/jbio.202000129. [PubMed: 32475014]

(165). Yasuda M; Takeshita N; Shigeto S Deuterium-Labeled Raman Tracking of Glucose Accumulation and Protein Metabolic Dynamics in Aspergillus Nidulans Hyphal Tips. Sci. Rep 2021, 11 (1), 1279. 10.1038/s41598-020-80270-9. [PubMed: 33446770]

(166). Hekmatara M; Heidari Baladehi M; Ji Y; Xu J D2O-Probed Raman Microspectroscopy Distinguishes the Metabolic Dynamics of Macromolecules in Organellar Anticancer Drug Response. Anal. Chem 2021, 93 (4), 2125–2134. 10.1021/acs.analchem.0c03925. [PubMed: 33435684]

(167). Zhao Z; Chen C; Xiong H; Ji J; Min W Metabolic Activity Phenotyping of Single Cells with Multiplexed Vibrational Probes. Anal. Chem 2020, 92 (14), 9603–9612. 10.1021/acs.analchem.0c00790. [PubMed: 32530266]

(168). Yang K; Li H-Z; Zhu X; Su J-Q; Ren B; Zhu Y-G; Cui L Rapid Antibiotic Susceptibility Testing of Pathogenic Bacteria Using Heavy-Water-Labeled Single-Cell Raman Spectroscopy in Clinical Samples. Anal. Chem 2019, 91 (9), 6296–6303. 10.1021/acs.analchem.9b01064. [PubMed: 30942570]

(169). Yi X; Song Y; Xu X; Peng D; Wang J; Qie X; Lin K; Yu M; Ge M; Wang Y; Zhang D; Yang Q; Wang M; Huang WE Development of a Fast Raman-Assisted Antibiotic Susceptibility Test (FRAST) for the Antibiotic Resistance Analysis of Clinical Urine and Blood Samples. Anal. Chem 2021, 93 (12), 5098–5106. 10.1021/acs.analchem.0c04709. [PubMed: 33728890]

(170). Hong W; Karanja CW; Abutaleb NS; Younis W; Zhang X; Seleem MN; Cheng J-X Antibiotic Susceptibility Determination within One Cell Cycle at Single-Bacterium Level by Stimulated Raman Metabolic Imaging. Anal. Chem 2018, 90 (6), 3737–3743. 10.1021/acs.analchem.7b03382. [PubMed: 29461044]

(171). Zhang W; Li Y; Yao L; Wu F; Chen C; Zhou L; Zheng B; Wang P; Hong W Rapid Antimicrobial Susceptibility Testing by Stimulated Raman Scattering Metabolic Imaging and Morphological Deformation of Bacteria. Anal. Chim. Acta 2021, 1168, 338622. 10.1016/j.aca.2021.338622. [PubMed: 34051990]

(172). Sun B; Kang X; Yue S; Lan L; Li R; Chen C; Zhang W; He S; Zhang C; Fan Y; Wang P; Zheng G; Hong W A Rapid Procedure for Bacterial Identification and Antimicrobial Susceptibility Testing Directly from Positive Blood Cultures. Analyst 2022, 147 (1), 147–154. 10.1039/D1AN01210J.

(173). Zhang W; Chen X; Zhang J; Chen X; Zhou L; Wang P; Hong W Rapid Antimicrobial Susceptibility Testing for Mixed Bacterial Infection in Urine by AI-Stimulated Raman Scattering Metabolic Imaging. Med. Nov. Technol. Devices 2022, 16, 100132. 10.1016/j.medntd.2022.100132.

(174). Zhang M; Hong W; Abutaleb NS; Li J; Dong PT; Zong C; Wang P; Seleem MN; Cheng JX Rapid Determination of Antimicrobial Susceptibility by Stimulated Raman Scattering Imaging of D2O Metabolic Incorporation in a Single Bacterium. Adv. Sci 2020, 7 (19), 2001452. 10.1002/ADVS.202001452.

(175). Chen C; Wang Y; Wu F; Hong W Rapid Antifungal Susceptibility Testing Based on Single-Cell Metabolism Analysis Using Stimulated Raman Scattering Imaging. Anal. Chem 2023, 95 (42), 15556–15565. 10.1021/acs.analchem.3c02243. [PubMed: 37815933]

(176). Zhang M; Hong W; Abutaleb NS; Li J; Dong P-T; Zong C; Wang P; Seleem MN; Cheng J-X Rapid Determination of Antimicrobial Susceptibility by Stimulated Raman Scattering Imaging of D2O Metabolic Incorporation in a Single Bacterium. Adv. Sci 2020, 7 (19), 2001452. 10.1002/advs.202001452.

(177). Huang K-C; Li J; Zhang C; Tan Y; Cheng J-X Multiplex Stimulated Raman Scattering Imaging Cytometry Reveals Lipid-Rich Protrusions in Cancer Cells under Stress Condition. iScience 2020, 23 (3), 100953. 10.1016/j.isci.2020.100953. [PubMed: 32179477]

(178). Tan Y; Li J; Zhao G; Huang K-C; Cardenas H; Wang Y; Matei D; Cheng J-X Metabolic Reprogramming from Glycolysis to Fatty Acid Uptake and Beta-Oxidation in Platinum-Resistant Cancer Cells. Nat. Commun 2022, 13 (1), 4554. 10.1038/s41467-022-32101-w. [PubMed: 35931676]

(179). Xu FX; Wu R; Hu K; Fu D Measuring Drug Response with Single-Cell Growth Rate Quantification. Anal. Chem 2023, 95 (49), 18114–18121. 10.1021/acs.analchem.3c03434. [PubMed: 38016067]

(180). Paudel A; Raijada D; Rantanen J Raman Spectroscopy in Pharmaceutical Product Design. Adv. Drug Deliv. Rev 2015, 89, 3–20. 10.1016/j.addr.2015.04.003. [PubMed: 25868453]

(181). Gala U; Chauhan H Principles and Applications of Raman Spectroscopy in Pharmaceutical Drug Discovery and Development. Expert Opin. Drug Discov 2015, 10 (2), 187–206. 10.1517/17460441.2015.981522. [PubMed: 25399993]

(182). Ralbovsky NM; Smith JP Raman Spectroscopy and Multivariate Analysis for Identification and Classification of Pharmaceutical Pain Reliever Tablets. J. Chemom 2023, 37 (3), e3429. 10.1002/cem.3429.

(183). Rebiere H; Martin M; Ghyselinck C; Bonnet P-A; Brenier C Raman Chemical Imaging for Spectroscopic Screening and Direct Quantification of Falsified Drugs. J. Pharm. Biomed. Anal 2018, 148, 316–323. 10.1016/j.jpba.2017.10.005. [PubMed: 29080412]

(184). Iwata K; Karashima M; Ikeda Y; Inoue M; Fukami T Discrimination and Quantification of Sulfathiazole Polytypes Using Low-Frequency Raman Spectroscopy. CrystEngComm 2018, 20 (14), 1928–1934. 10.1039/C8CE00081F.

(185). Coic L; Sacré P-Y; Dispas A; De Bleye C; Fillet M; Ruckebusch C; Hubert P; Ziemons E Pixel-Based Raman Hyperspectral Identification of Complex Pharmaceutical Formulations. Anal. Chim. Acta 2021, 1155, 338361. 10.1016/j.aca.2021.338361. [PubMed: 33766319]

(186). Venkatesan A; Radhakrishnan A; Kuppuswamy G; Singh SK Detectability & Quantification of Low-Dose Glimepiride in a Fixed-Dose Combination Using Raman Imaging. Vib. Spectrosc 2021, 113, 103229. 10.1016/j.vibspec.2021.103229.

(187). Carruthers H; Clark D; Clarke F; Faulds K; Graham D Comparison of Raman and Near-Infrared Chemical Mapping for the Analysis of Pharmaceutical Tablets. Appl. Spectrosc 2021, 75 (2), 178–188. 10.1177/0003702820952440. [PubMed: 32757763]

(188). Ohashi R; Fujii A; Fukui K; Koide T; Fukami T Non-Destructive Quantitative Analysis of Pharmaceutical Ointment by Transmission Raman Spectroscopy. Eur. J. Pharm. Sci 2022, 169, 106095. 10.1016/j.ejps.2021.106095. [PubMed: 34906685]

(189). Nilsson N; Nezvalova-Henriksen K; Bøtker JP; Højmark Andersen N; Strøm Larsen B; Rantanen J; Tho I; Brustugun J Co-Administration of Intravenous Drugs: Rapidly Troubleshooting the Solid Form Composition of a Precipitate in a Multi-Drug Mixture

Using On-Site Raman Spectroscopy. Mol. Pharm 2023, 20 (6), 2853–2863. 10.1021/acs.molpharmaceut.2c00983. [PubMed: 37167030]

(190). Lee EH A Practical Guide to Pharmaceutical Polymorph Screening & Selection. Asian J. Pharm. Sci 2014, 9 (4), 163–175. 10.1016/j.ajps.2014.05.002.

(191). Grand C; Scotté C; Rigneault H Fast Compressive Raman Imaging of Polymorph Molecules and Excipients in Pharmaceutical Tablets. Anal. Chem 2022, 94 (48), 16632–16637. 10.1021/acs.analchem.2c02680. [PubMed: 36417695]

(192). Fateixa S; Nogueira HIS; Trindade T Carbamazepine Polymorphism: A Re-Visitation Using Raman Imaging. Int. J. Pharm 2022, 617, 121632. 10.1016/j.ijpharm.2022.121632. [PubMed: 35245634]

(193). Šašić S; Prusnick T Raman Chemical Imaging of Intact Non-Flat Tablets in Regular and High-Confocal Mode. Anal. Methods 2020, 12 (4), 471–482. 10.1039/C9AY02340B.

(194). Koutentaki G; Krýsa P; Trunov D; Pekárek T; Pišlová M; Šoóš M 3D Raman Mapping as an Analytical Tool for Investigating the Coatings of Coated Drug Particles. J. Pharm. Anal 2023, 13 (3), 276–286. 10.1016/j.jpha.2023.02.004. [PubMed: 37102110]

(195). Brock D; Zeitler JA; Funke A; Knop K; Kleinebudde P Evaluation of Critical Process Parameters for Intra-Tablet Coating Uniformity Using Terahertz Pulsed Imaging. Eur. J. Pharm. Biopharm 2013, 85 (3, Part B), 1122–1129. 10.1016/j.ejpb.2013.07.004. [PubMed: 23872179]

(196). Carruthers H; Clark D; Clarke FC; Faulds K; Graham D Three-Dimensional Imaging of Pharmaceutical Tablets Using Serial Sectioning and Raman Chemical Mapping. J. Raman Spectrosc 2022, 53 (6), 1115–1125. 10.1002/jrs.6337.

(197). Inoue M; Osada T; Hisada H; Koide T; Fukami T; Roy A; Carriere J; Heyler R Solid-State Quantification of Cocrystals in Pharmaceutical Tablets Using Transmission Low-Frequency Raman Spectroscopy. Anal. Chem 2019, 91 (21), 13427–13432. 10.1021/acs.analchem.9b01895. [PubMed: 31565923]

(198). Inoue M; Hisada H; Koide T; Fukami T; Roy A; Carriere J; Heyler R Transmission Low-Frequency Raman Spectroscopy for Quantification of Crystalline Polymorphs in Pharmaceutical Tablets. Anal. Chem 2019, 91 (3), 1997–2003. 10.1021/acs.analchem.8b04365. [PubMed: 30606009]

(199). Song SW; Kim J; Eum C; Cho Y; Park CR; Woo Y-A; Kim HM; Chung H Hyperspectral Raman Line Mapping as an Effective Tool To Monitor the Coating Thickness of Pharmaceutical Tablets. Anal. Chem 2019, 91 (9), 5810–5816. 10.1021/acs.analchem.9b00047. [PubMed: 30916927]

(200). Bērziņš K; Fraser-Miller SJ; Gordon KC Pseudo-3D Subsurface Imaging of Pharmaceutical Solid Dosage Forms Using Micro-Spatially Offset Low-Frequency Raman Spectroscopy. Anal. Chem 2021, 93 (25), 8986–8993. 10.1021/acs.analchem.1c01670. [PubMed: 34142802]

(201). Bērziņš K; Fraser-Miller SJ; Gordon KC A New Frontier for Nondestructive Spatial Analysis of Pharmaceutical Solid Dosage Forms: Spatially Offset Low-Frequency Raman Spectroscopy. Anal. Chem 2021, 93 (8), 3698–3705. 10.1021/acs.analchem.0c04960. [PubMed: 33590756]

(202). Fateixa S; Mulandeza O; Nogueira HIS; Trindade T Raman Imaging Studies on the Stability of Paracetamol Tablets under Different Storage Conditions. Vib. Spectrosc 2023, 124, 103488. 10.1016/j.vibspec.2022.103488.

(203). Abouselo A; Rance GA; Tres F; Taylor LS; Kwokal A; Renou L; Scurr DJ; Burley JC; Aylott JW Effect of Excipients on Salt Disproportionation during Dissolution: A Novel Application of In Situ Raman Imaging. Mol. Pharm 2021, 18 (9), 3247–3259. 10.1021/acs.molpharmaceut.1c00119. [PubMed: 34399050]

(204). Galata DL; Zsiros B; Knyihár G; Péterfi O; Mészáros LA; Ronkay F; Nagy B; Szabó E; Nagy ZK; Farkas A Convolutional Neural Network-Based Evaluation of Chemical Maps Obtained by Fast Raman Imaging for Prediction of Tablet Dissolution Profiles. Int. J. Pharm 2023, 640, 123001. 10.1016/j.ijpharm.2023.123001. [PubMed: 37254287]

(205). Galata DL; Zsiros B; Mészáros LA; Nagy B; Szabó E; Farkas A; Nagy ZK Raman Mapping-Based Non-Destructive Dissolution Prediction of Sustained-Release Tablets. J. Pharm. Biomed. Anal 2022, 212, 114661. 10.1016/j.jpba.2022.114661. [PubMed: 35180565]

(206). Francis AT; Nguyen TT; Lamm MS; Teller R; Forster SP; Xu W; Rhodes T; Smith RL; Kuiper J; Su Y; Fu D In Situ Stimulated Raman Scattering (SRS) Microscopy Study of the

Dissolution of Sustained-Release Implant Formulation. Mol. Pharm 2018, 15 (12), 5793–5801. 10.1021/acs.molpharmaceut.8b00965. [PubMed: 30362772]

(207). Figueroa B; Nguyen T; Sotthivirat S; Xu W; Rhodes T; Lamm MS; Smith RL; John CT; Su Y; Fu D Detecting and Quantifying Microscale Chemical Reactions in Pharmaceutical Tablets by Stimulated Raman Scattering Microscopy. Anal. Chem 2019. 10.1021/acs.analchem.9b01269.

(208). Wei Y; Pence IJ; Wiatrowski A; Slade JB; Evans CL Quantitative Analysis of Drug Tablet Aging by Fast Hyper-Spectral Stimulated Raman Scattering Microscopy. Analyst 2024, 149 (5), 1436–1446. 10.1039/D3AN01527K. [PubMed: 38050860]

(209). Wong B; Zhao X; Su Y; Ouyang H; Rhodes T; Xu W; Xi H; Fu D Characterizing Silicone Oil-Induced Protein Aggregation with Stimulated Raman Scattering Imaging. Mol. Pharm 2023, 20 (8), 4268–4276. 10.1021/acs.molpharmaceut.3c00391. [PubMed: 37382286]

(210). Slipchenko MN; Le TT; Chen H; Cheng J-X High-Speed Vibrational Imaging and Spectral Analysis of Lipid Bodies by Compound Raman Microscopy. J. Phys. Chem. B 2011, 113 (21), 7681–7686. 10.1021/jp902231y.

(211). Camp CH Jr; Lee YJ; Heddleston JM; Hartshorn CM; Walker ARH; Rich JN; Lathia JD; Cicerone MT High-Speed Coherent Raman Fingerprint Imaging of Biological Tissues. Nat. Photonics 2014, 8 (8), 627–634. 10.1038/nphoton.2014.145. [PubMed: 25621002]

(212). Hashimoto K; Takahashi M; Ideguchi T; Goda K Broadband Coherent Raman Spectroscopy Running at 24,000 Spectra per Second. Sci. Rep 2016, 6 (1), 21036. 10.1038/srep21036. [PubMed: 26875786]

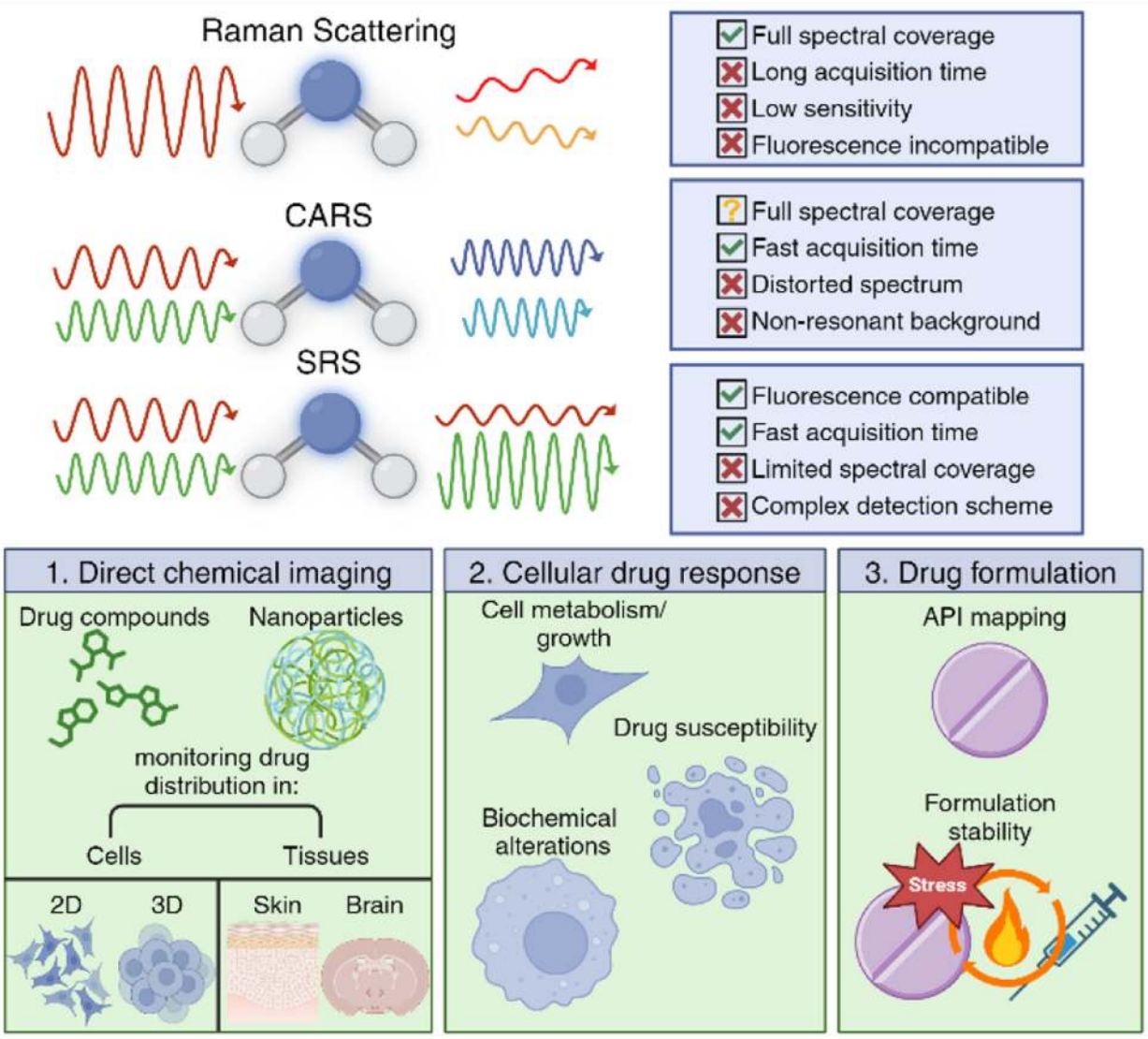

Figure 1.

Top: brief advantages and disadvantages of spontaneous Raman scattering and coherent Raman techniques (CARS and SRS). Bottom: applications of Raman techniques on pharmaceutical drugs to visualize drug distribution, drug response, and drug formulation. Created with BioRender.com

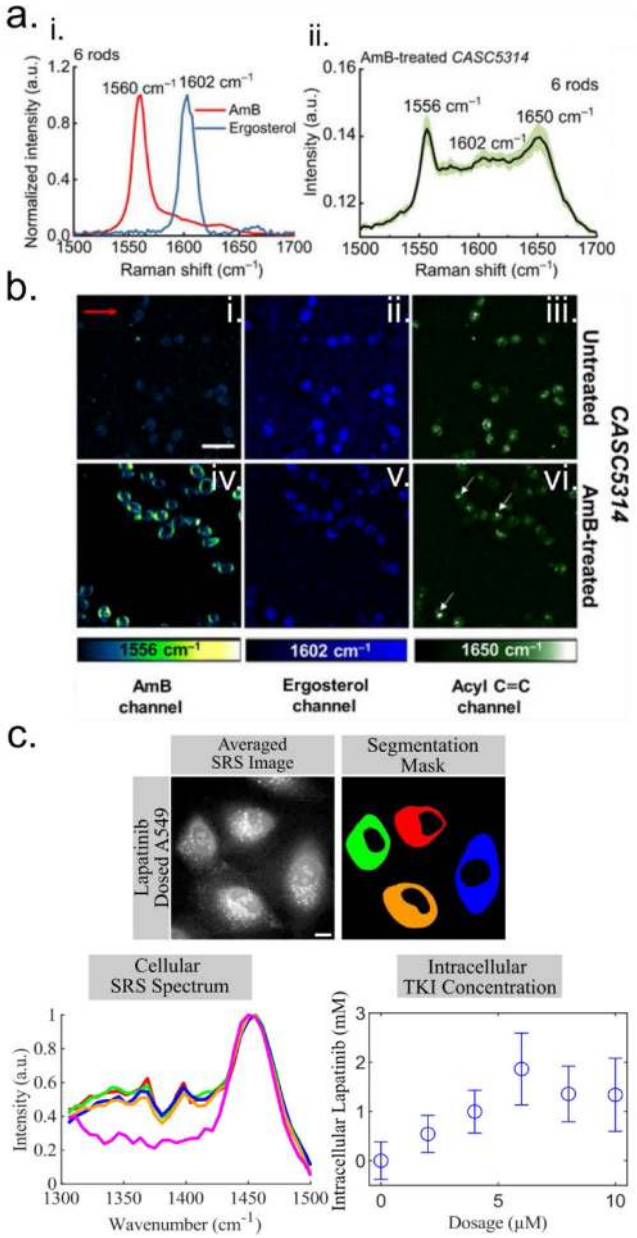

Figure 2.

Direct imaging of intracellular drug uptake. a. (i.) SRS spectra of AmB (10 mg/ml) and pure ergosterol, with optimal Raman peaks highlighted. Data acquired under six-rod chirping. (ii.) SRS spectra of single AmB-treated CASC5314 cells. Data: means ± SD from at least 10 yeasts. AmB: 3.2 μg/ml for 1 h. Data acquired under six-rod chirping condition. b. (i.-iii.) SRS images of untreated CASC5314 cells at 1556, 1602, and 1650 cm^{-1}, respectively. (iv.-vi.) SRS images of AmB-treated CASC5314 cells at 1556, 1602, and 1650 cm^{-1}, respectively. Pixel dwell time: 50 μs. Scale bar, 10 μm. Laser polarization direction is indicated by red arrows. Lipid droplet is indicated by white arrows. From Dong, P.-T.; Zong, C.; Dagher, Z.; Hui, J.; Li, J.; Zhan, Y.; Zhang, M.; Mansour, M. K.; Cheng, J.-X. Polarization-Sensitive Stimulated Raman Scattering Imaging Resolves Amphotericin B

Orientation in Candida Membrane. Sci. Adv. 2021, 7 (2), eabd5230. (ref 87) Reprinted with permission from AAAS. c. Top, left to right: average intensity SRS image of A549 cells treated with 4 μM lapatinib for 4 h before imaging between 1300–1500 cm^{-1}; cell cytoplasm segmentation mask generated by Cellpose for a per-cell SRS spectrum; Bottom, left to right: cytoplasmic SRS spectra of the respective cells colored in segmentation mask. The spectrum in magenta represents an average DMSO-d_6-dosed control cell; plot of intracellular lapatinib concentration measurement across 4 h treatments with a concentration gradient from 2 to 10 μM lapatinib. Reproduced from Wong, B. S.; Dunnington, E. L.; Wu, R.; Kim, J. I.; Hu, K.; Ro, T. H.; Fu, D. Facilitated Transport of EGFR Inhibitors Plays an Important Role in Their Cellular Uptake. Anal. Chem. 2024, 96 (4), 1547–1555. (ref 88). Copyright 2024 American Chemical Society.

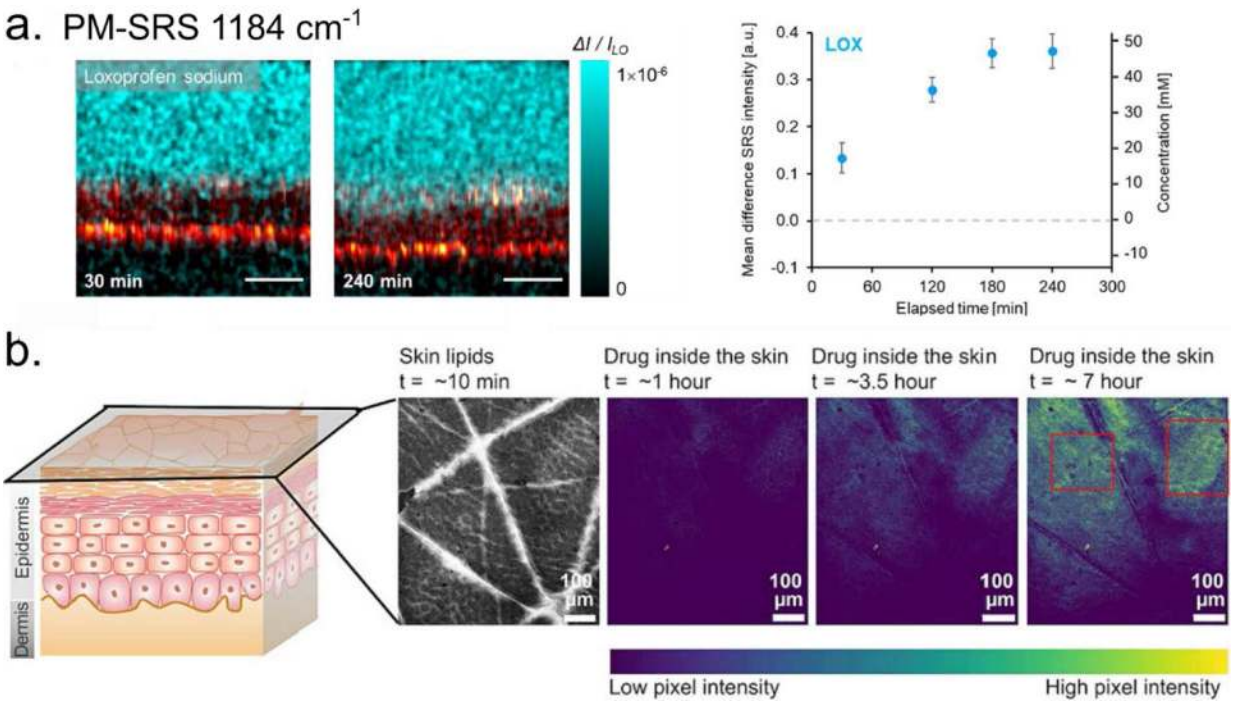

Figure 3.

Drug uptake into skin. a. Skin penetration analysis of topically applied drugs with PM-SRS. Left: PM-SRS X-Z plane images of 4% (131 mM) loxoprofen sodium salt (1184 cm^{-1}) permeation into skin from 30 min to 240 min after application where $\Delta I / ILO$ indicates SRS signal intensity. SRS chemical maps are superimposed over confocal-reflection images (orange) to visualize skin structure. Scale bar, 50 µm. Right: mean difference SRS intensity of 4% loxoprofen sodium salt (1184 cm^{-1}) permeation into a skin model. Lox: loxoprofen sodium. Reprinted with permission from ref 111 © Optica Publishing Group. b. SRS images tracking tazarotene uptake (1590 cm^{-1}) at 8 µm depth from 10 min to 7 h, where a shift in higher pixel intensity (blue to yellow) indicates higher drug content. Tazarotene and lipid (2870 cm^{-1}) content were overlayed to track drug distribution. Red box: drug permeation through lipid-rich intercellular lamellae regions. Reprinted from J. Controlled Release., Vol. 367, Iliopoulos, F.; Tu, D.; Pence, I. J.; Li, X.; Ghosh, P.; Luke, M. C.; Raney, S. G.; Rantou, E.; Evans, C. L. Determining Topical Product Bioequivalence with Stimulated Raman Scattering Microscopy, pp. 864–876 (ref 114). Copyright 2024, with permission from Elsevier.

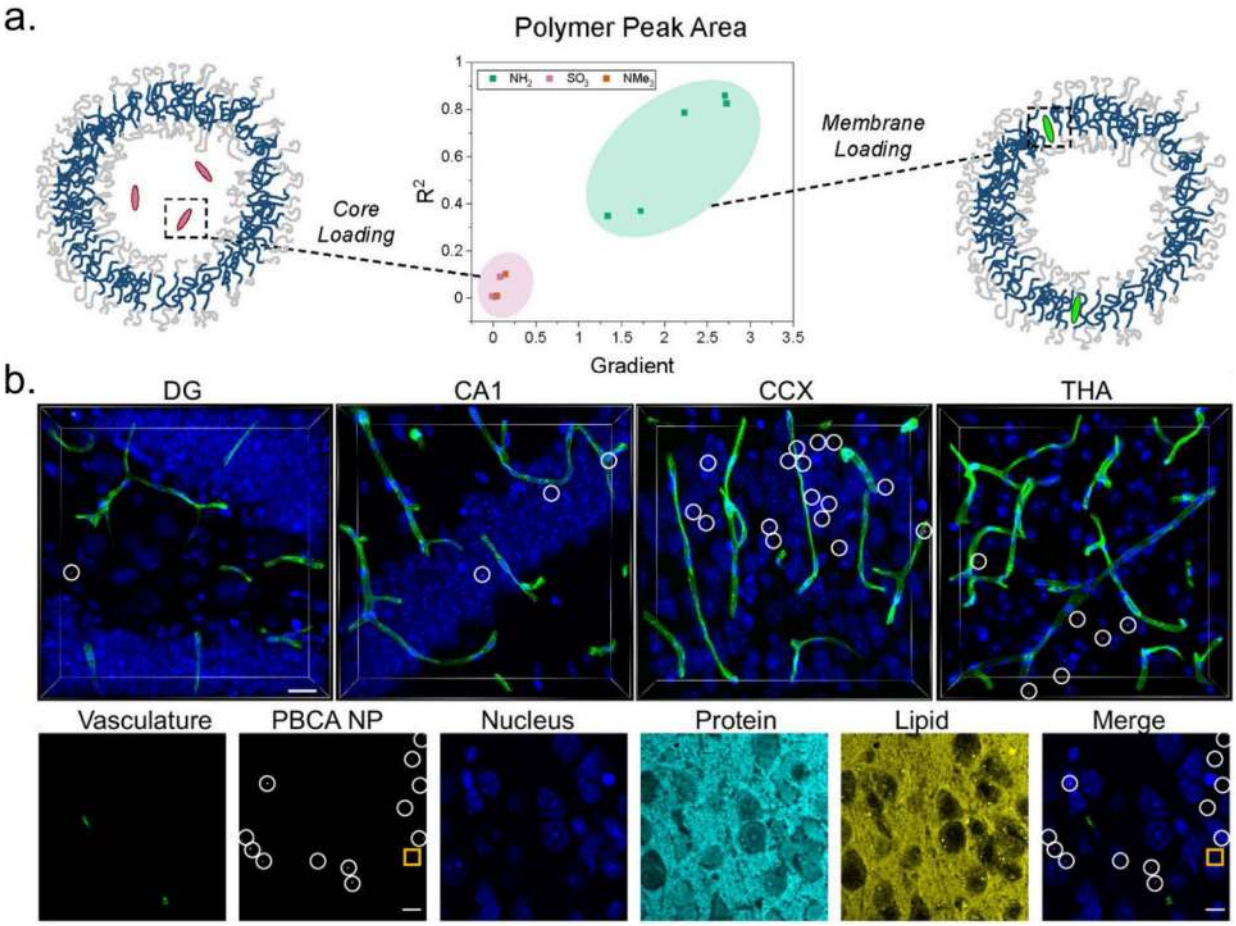

Figure 4.

Imaging nanocarrier-based therapeutics. a. Distinguishing cargo loading location using single particle measurements from SPARTA data. Summary of analytical framework. By extracting the R^2 and gradient from linear fits of cargo-carrier scatter plots, membrane and core loading can be distinguished: core loading causes low gradient and low R^2, so particles appear in the lower left quadrant. Meanwhile, membrane loading is characterized by high R^2 and high gradient, so particles appear in the upper right quadrant. Ovals are drawn to aid interpretation. Reprinted with permission from Saunders, C.; Foote, J. E. J.; Wojciechowski, J. P.; Cammack, A.; Pedersen, S. V.; Doutch, J. J.; Barriga, H. M. G.; Holme, M. N.; Penders, J.; Chami, M.; Najer, A.; Stevens, M. M. Revealing Population Heterogeneity in Vesicle-Based Nanomedicines Using Automated, Single Particle Raman Analysis. ACS Nano 2023, 17 (12), 11713–11728. (ref 129). Copyright 2023 American Chemical Society. b. Single-particle counting of PBCA nanoparticles that cross the BBB. Top: volume-rendered images of nanoparticles, vasculature, and nuclei in different brain regions. The cerebral cortex (CCX); the dentate gyrus of the hippocampus (DG); the CA1 region of the hippocampus (CA1); and the thalamus (THA). Circles indicate nanoparticle spots. Bottom: single-plane images of nanoparticles, proteins, lipids, vasculature, and nuclei in the cerebral cortex. Circles indicate nanoparticle spots. Scale bars: 20 μm in (i.), 10 μm in (ii.) Reproduced with permission from *Proceedings of the National Academy of Sciences USA* Wei, M.; Qian, N.; Gao, X.; Lang, X.; Song, D.; Min, W. Single-Particle Imaging of

Nanomedicine Entering the Brain. Proc. Natl. Acad. Sci. 2024, 121 (5), e2309811121 (ref 134).

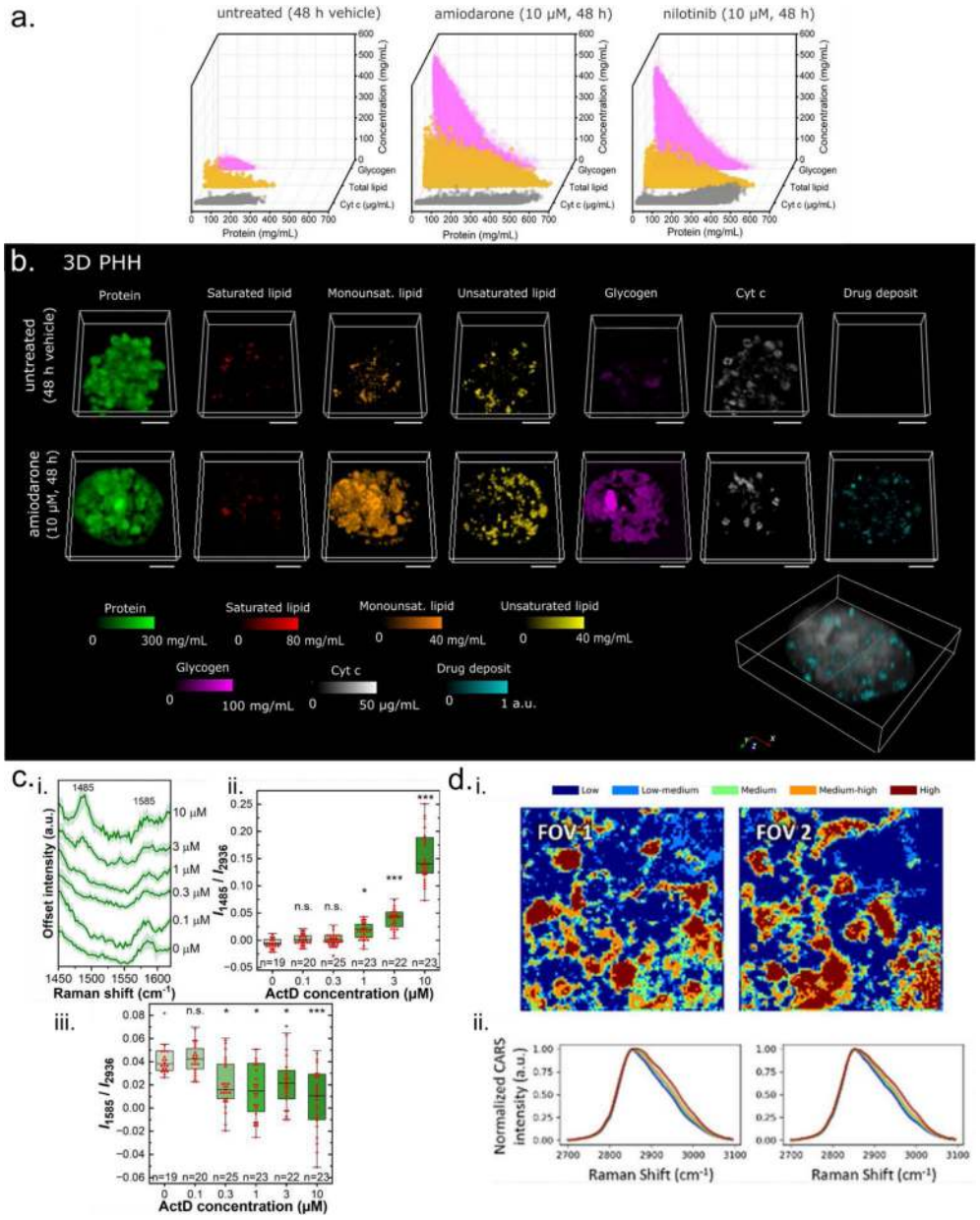

Figure 5.

Platforms to monitor drug-induced biochemical alterations. a. Frequency distribution plots of total lipid, glycogen, and cytochrome c vs. protein content for representative drug-treated samples. High-content chemometric profiling of individual control (48 h of vehicle treatment). b. Untreated and amiodarone-treated (10 μM, 48 h) 3D PHH spheroids. Amiodarone induces significant measurable changes in biomolecular composition of both 3D liver representations. 3D renderings of amiodarone and metabolites deposits (shown in cyan) detected in PHH spheroids and iHLC organoids. The biomolecular matrix (i.e., protein, total lipid, and glycogen) was combined and is shown in gray (arbitrary intensity units) to reveal a clear distinction between endogenous biomolecules and xenobiotic compounds present in specimens. Scale bars, 50 μm. Reprinted from Cell Rep. Methods,

Vol. 3 (4), LaLone, V.; Aizenshtadt, A.; Goertz, J.; Skottvoll, F. S.; Mota, M. B.; You, J.; Zhao, X.; Berg, H. E.; Stokowiec, J.; Yu, M.; Schwendeman, A.; Scholz, H.; Wilson, S. R.; Krauss, S.; Stevens, M. M. Quantitative Chemometric Phenotyping of Three-Dimensional Liver Organoids by Raman Spectral Imaging, pp. 100440 (ref 152). Copyright 2023, with permission from Elsevier. c. Raman observation of the drug effect of HeLa spheroids under a range of drug concentration treatments (0–10 μM). (i.) Raman spectra of ActD-treated HeLa spheroids. The solid lines indicate the mean values, and the SDs are shown in light green. The boxplots of the Raman intensities at (ii.) 1485 cm^{-1} (assigned to ActD) and (iii.) 1585 cm^{-1} (assigned to cyt c) normalized by dividing by 2936 cm^{-1} (as reference for detected volume in spheroids) reveal a dose-dependent intensities change. The boxplots illustrate the internal data points (center line: median, box: quartiles, low/up whiskers: max/min value in 1.5 interquartile range). A significant difference was compared with the leftmost box. ***: $P < 0.001$; *: $P < 0.05$; n.s.: $P > 0.05$. Reproduced from Liao, H.-X.; Bando, K.; Li, M.; Fujita, K. Multifocal Raman Spectrophotometer for Examining Drug-Induced and Chemical-Induced Cellular Changes in 3D Cell Spheroids. Anal. Chem. 2023, 95 (39), 14616–14623. (ref 154). Copyright 2023 American Chemical Society. d. CARS spectral profiles of regions at different attention levels. (i.) By quantizing the attention scores to five levels, the attention heatmaps were divided into five attention-ranked regions (i.e., low, low-medium, medium, medium-high, and high). The normalized CARS spectral profiles of regions at different attention levels are shown in (ii.). Reproduced from Shi, J.; Bera, K.; Mukherjee, P.; Alex, A.; Chaney, E. J.; Spencer-Dene, B.; Majer, J.; Marjanovic, M.; Spill-man, D. R. J.; Hood, S. R.; Boppart, S. A. Weakly Supervised Identification and Localization of Drug Fingerprints Based on Label-Free Hyperspectral CARS Microscopy. Anal. Chem. 2023, 95 (29), 10957–10965. (ref 160). Copyright 2023 American Chemical Society.

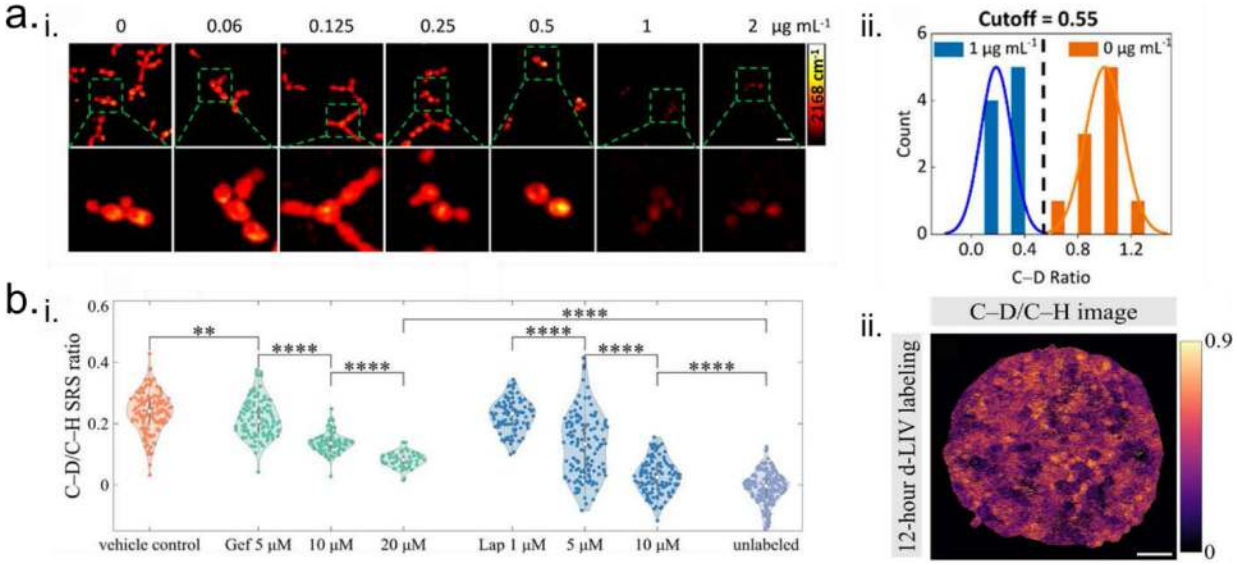

Figure 6.

Tracing single-cell metabolic response with Raman isotopic labels. a. SRS imaging for single-cell rapid antifungal susceptibility testing (AFST). (i.) C−D (2168 cm^{-1}) SRS images of susceptible *Candida albicans* cells treated with increasing concentrations of amphotericin B. Scale bar, 20 μm. (ii.) Histogram of C−D intensities for the drug-treated group indicating significant metabolic change (1 μg/mL) in blue and drug-free group in orange. Plots were fitted with normal distributions of the drug-free group. A cutoff threshold of 0.55 was found for separating the two groups. Reproduced from Chen, C.; Wang, Y.; Wu, F.; Hong, W. Rapid Antifungal Susceptibility Testing Based on Single-Cell Metabolism Analysis Using Stimulated Raman Scattering Imaging. Anal. Chem. 2023, 95 (42), 15556–15565. (ref 175). Copyright 2023 American Chemical Society. b. Ratiometric C−D/C−H SRS ratios as a cell growth rate measurement. (i.) Cell growth measurement of single A549 cells treated with increasing concentrations of gefitinib (Gef) and lapatinib (Lap) with DMSO as a vehicle control. Images were collected after 12 h of drug dosing with 4 h d-LIV labeling. Each point represents one whole cell. Response subpopulations at 5 μM lapatinib are observed. Significance: **: $p \leq 0.01$, ****: $p \leq 0.0001$. (ii.) Growth rate variation within an A549 3D spheroid after 12 h d-LIV labeling visualized with ratiometric C−D/C−H SRS imaging. Scale bar, 50 μm. Reproduced from Xu, F. X.; Wu, R.; Hu, K.; Fu, D. Measuring Drug Response with Single-Cell Growth Rate Quantification. Anal. Chem. 2023, 95 (49), 18114–18121. (ref 179). Copyright 2023 American Chemical Society.

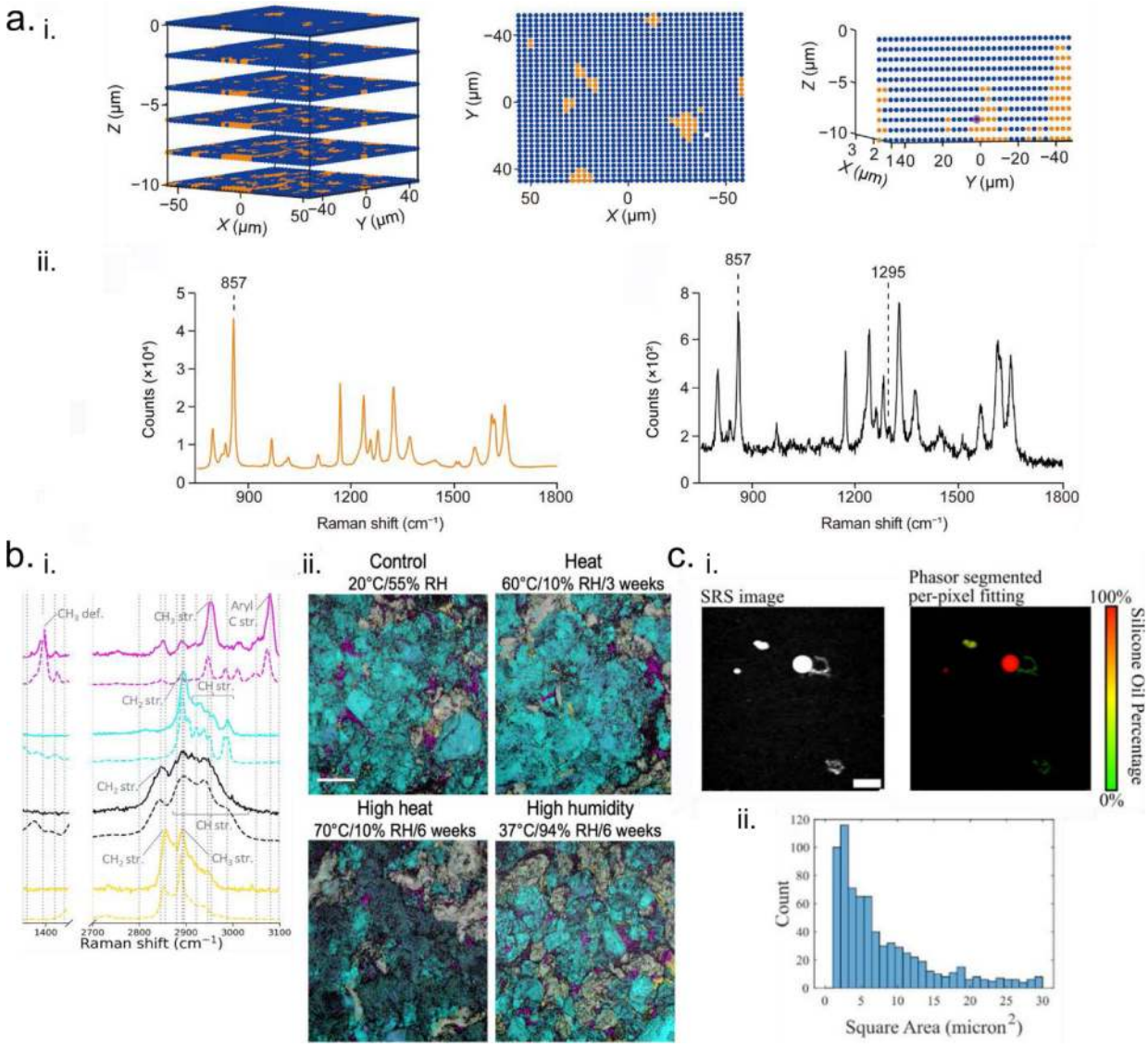

Figure 7.

Visualization of drug product components and dynamic changes. a. 3D sections of inner layers of dry-coated drug particles. (i.) Left: 200–400 μm fraction layer of dry-coated paracetamol particle, with paracetamol (857 cm^{-1}) in orange and carnauba wax (1295 cm^{-1}) in blue. Carnauba wax appears most prominently in the top z planes. Middle: x-y plane of top z layer of particle fraction. Right: x-plane of coated particle. (ii.) Raman spectra of pure paracetamol (orange, left) and the pixel labeled in pink in (i.) (black, right). Reprinted from J. Pharm. Anal., Vol. 13, Koutentaki, G.; Krýsa, P.; Trunov, D.; Pekárek, T.; Pišlová, M.; Šoóš, M. 3D Raman Mapping as an Analytical Tool for Investigating the Coatings of Coated Drug Particles, pp. 276–286 (ref 194). Copyright 2023, with permission from Elsevier B.V. on behalf of Xi'an Jiaotong University. b. Quantification of drug tablet aging with SRS imaging. (i.) SRS (solid) and spontaneous (dotted) spectra of tablet components: pure naproxen (magenta), lactose (cyan), HPMC (white), and Mgst (yellow), respectively, spectrally unmixed from a naproxen tablet cross-section. def.: deformation, str.: stretching.

(ii.) Tablet cross-section SRS composite abundance maps (top row) and thresholded images (bottom row) with accelerating tablet aging conditions using the color scheme from (i.). Scale bar, 100 μm. Reproduced from Wei, Y.; Pence, I. J.; Wiatrowski, A.; Slade, J. B.; Evans, C. L. Quantitative Analysis of Drug Tablet Aging by Fast Hyper-Spectral Stimulated Raman Scattering Microscopy. Analyst 2024, 149 (5), 1436–1446 (ref 208), with permission of The Royal Society of Chemistry. c. Silicone oil-induced particle aggregation in a stressed therapeutic solution. (i.) Averaged C–H region (2800–3060 cm^{-1}) SRS image and phasor pixel-based segmentation with least squares regression fitting of silicone oil- and protein-containing particles on a polycarbonate filter. In phasor image, green: protein content (2930 cm^{-1}), red: silicone oil (2900 cm^{-1}) content. Scale bar, 15 μm. (ii.) Size distribution of 911 particles segmented out by phasor analysis. Reproduced from Wong, B.; Zhao, X.; Su, Y.; Ouyang, H.; Rhodes, T.; Xu, W.; Xi, H.; Fu, D. Characterizing Silicone Oil-Induced Protein Aggregation with Stimulated Raman Scattering Imaging. Mol. Pharm. 2023, 20 (8), 4268–4276. (ref 209). Copyright 2023 American Chemical Society.